THE EUROPEAN
PHYSICAL JOURNAL C

The CMSSM survives *Planck*, the LHC, LUX-ZEPLIN, *Fermi*-LAT, H.E.S.S. and IceCube

John Ellis[1,2,3], **Keith A. Olive**[4], **Vassilis C. Spanos**[5,a], **Ioanna D. Stamou**[6]

[1] Theoretical Particle Physics and Cosmology Group, Department of Physics, King's College London, London WC2R 2LS, UK
[2] Theoretical Physics Department, CERN, 1211 Geneva 23, Switzerland
[3] National Institute of Chemical Physics and Biophysics, Rävala 10, 10143 Tallinn, Estonia
[4] William I. Fine Theoretical Physics Institute, School of Physics and Astronomy, University of Minnesota, Minneapolis, MN 55455, USA
[5] Section of Nuclear and Particle Physics, Department of Physics, National and Kapodistrian University of Athens, 157 84 Athens, Greece
[6] Service de Physique Théorique, Université Libre de Bruxelles, Boulevard du Triomphe CP225, 1050 Brussels, Belgium

Abstract We revisit the viability of the CMSSM, searching for regions of parameter space that yield a neutralino dark matter density compatible with *Planck* measurements, as well as LHC constraints including sparticle searches and the mass of the Higgs boson, recent direct limits on spin-independent and -dependent dark matter scattering from the LUX-ZEPLIN (LZ) experiment, the indirect constraints from *Fermi*-LAT and H.E.S.S. on dark matter annihilations to photons in dwarf spheroidal galaxies and the Galactic Centre, and the IceCube limits on muons from annihilations to neutrinos in the Sun. For representative values of $\tan \beta$ and A_0 we map in detail the *Planck*-compatible strips in CMSSM parameter planes, which exhibit multiple distinctive features for large $\tan \beta$, $A_0 = 0$ and $\mu > 0$, and identify portions of the strips that survive all the phenomenological constraints. We find that the most powerful constraint is that from m_h, followed by the LZ limit on spin-independent scattering, whereas sparticle searches at the LHC and indirect dark matter searches are less restrictive. Most of the surviving CMSSM parameter space features a Higgsino-like dark matter particle with a mass $\sim 1000-1100$ GeV, which could best be probed with future direct searches for dark matter scattering.

1 Introduction

The Constrained Supersymmetric extension of the Standard Model (CMSSM) is a commonly-used template for supersymmetry phenomenology [1–16], which incorporates the simplified assumption that the soft supersymmetry-breaking parameters are universal at the gauge coupling unification scale $\sim 10^{16}$ GeV. The CMSSM has often been used, for example, to interpret supersymmetry searches at the LHC and both direct and indirect searches for astrophysical dark matter.

The continuing lack of success in accelerator searches for supersymmetric particles [17–20] as well as searches for massive astrophysical dark matter particles [21–25] has been exerting ever-increasing pressure on supersymmetric models in general and the CMSSM in particular. The low dimensionality of the CMSSM parameter space enforces many links between supersymmetric observables and has relatively few unexplored corners. Under these circumstances, an ever more pressing question is whether the CMSSM survives all the phenomenological constraints. If it does, there is likely to be an ever-decreasing region of CMSSM parameter space where experimental searches should focus, which may be interesting also for more general supersymmetric models. If the CMSSM does not survive, the time has come to move on, either to more general supersymmetric models or to other scenarios for dark matter and complementary possibilities for physics beyond the Standard Model.

Our philosophy in this paper is to regard the CMSSM as the canary in the supersymmetric coalmine, whose survival is indicative of the general state of health of supersymmetric phenomenology. As we shall see, the CMSSM continues to survive the experimental onslaught in a restricted range of parameters that is quite vulnerable to upcoming direct searches for astrophysical dark matter.

The following are the phenomenological constraints that we consider in this paper.

The most restrictive is the constraint on the density of dark matter provided by the *Planck* satellite and other measure-

a e-mail: vspanos@phys.uoa.gr (corresponding author)

Springer

ments, which has percent-level precision [26]. Our calculation of the relic density assumes standard thermal freeze-out. However, it is subject to at least two important caveats. One is that the supersymmetric relic density will in general be changed if the expansion history is modified or if the late decay of a massive particle (which comes to dominate the energy density) adds entropy to the radiation bath after freeze-out [27,28] and the other is that there may be other sources of dark matter, in which case the supersymmetric relic density may be less than the total dark matter density indicated by *Planck* and other experiments. Nevertheless, we take the *Planck* dark matter density constraint at face value, commenting later on the extension of our results to the possibility that the LSP contributes only a fraction of the cold dark matter density.

The second most stringent constraint is provided by the mass of the Higgs boson, which has been measured at the per-mille level [29–31]. Theoretical calculations of m_h within supersymmetric models have estimated accuracies at the percent level. In our analysis we use calculations with the FeynHiggs 2.18.1 code [32], taking into account their estimated uncertainties. As we shall see, the m_h constraint is quite complementary to the *Planck* constraint.

Another set of constraints is provided by LHC searches for supersymmetric particles, which yield (so far) only lower limits on sparticle masses [17–20] and hence the CMSSM supersymmetry-breaking parameters m_0 (the supposedly universal scalar mass at the unification scale) and $m_{1/2}$ (the supposedly universal gaugino mass). In principle, these limits depend somewhat on the values of $\tan\beta$ (the ratio of supersymmetric Higgs vev's) and A_0 (the supposedly universal soft trilinear supersymmetry-breaking parameter). However, we find that the LHC constraints are not relevant in the regions of CMSSM parameter space favoured by the measurement of m_h, implying that a detailed implementation is not necessary.

We stress that our motivation for studying the CMSSM is the simplicity embodied in the assumptions on scalar and gaugino mass universality. Of course there are many more complicated extensions of this paradigm, such as models in which the Higgs masses differ from the scalar masses at the unification scale, which are commonly known as non-universal Higgs mass models (NUHM) [33–37]. Additional parameters will clearly relax the impact on the model imposed by experimental constraints. To the extent that the CMSSM survives them, other models will survive them more easily. As we will see, the CMSSM survives these constraints with a supersymmetry breaking mass scale that is $\mathcal{O}(10)$ TeV [38,39], larger than the scale originally associated with supersymmetry when it was proposed as a solution to the hierarchy problem [40–42]. However, supersymmetry at any scale below the GUT or Planck scale alleviates the hierarchy problem to some extent.

We implement several astrophysical constraints on dark matter interactions. The first are the direct upper limits on spin-independent and -dependent astrophysical dark matter scattering set recently by the LUX-ZEPLIN (LZ) experiment [25], which are more stringent than those set previously by the LUX [22], PANDA-X [23,24] and XENON [21] experiments. As we show later, the spin-independent scattering constraint excludes parts of the dark matter strips that are compatible with m_h, the other LHC and indirect dark matter constraints.

We also consider several indirect constraints on astrophysical dark matter annihilations [43,44]. The first is provided by upper limits from *Fermi*-LAT on γ fluxes from dwarf spheroidal satellite galaxies [45–50]. As discussed in [51] and in the text, we combine the γ flux limits from all the available dwarf data sets. As in the case of the LHC constraints, we find that the combined γ limit does not impact the region of parameter space favoured by m_h and the dark matter density. The same is true for the upper limits from the γ flux from the Galactic Centre [52–55]. The final indirect limit we consider is that on dark matter annihilation in the Sun [56–63] set by the IceCube search for energetic neutrinos from the Sun [64–66].

In order to set the stage for the applications of the different constraints, we first discuss in detail in Sect. 2 the dark matter strips for different values of $\tan\beta$, $A_0 = 0$ and $\mu > 0$ and the underlying mechanisms that play dominant roles in bringing the cosmological dark matter density into the range allowed by *Planck* and other measurements. These include the focus-point and well-tempered neutralino mechanisms, coannihilation between the LSP and other sparticles such as heavier neutralinos, charginos and stop squarks, and annihilations via s-channel heavy Higgs bosons (H/A). As we discuss in Sect. 2, these different mechanisms may combine constructively in non-trivial ways. The pattern of dark matter strips is richest when $\tan\beta \geq 40$, $A_0 = 0$ and $\mu > 0$, simplifying significantly to the focus-point strip for smaller $\tan\beta$ when $A_0 = 0$ and $\mu > 0$, to the stop coannihilation strip when $A_0 = 3\,m_0$ and $\mu > 0$, and again to the focus-point strip when $\mu < 0$.

Section 3 of this paper discusses the LHC constraints on the CMSSM when $A_0 = 0$ and $\mu > 0$, with particular focus on the m_h constraint, which is generally much more important than the direct searches for supersymmetric particles. We then discuss the astrophysical constraints on dark matter interactions when $A_0 = 0$ and $\mu > 0$ in Sect. 4, and combine these constraints in Sect. 5. As we discuss in more detail below, for most of the values of $\tan\beta$ that we study when $A_0 = 0$ and $\mu > 0$, there is a small region of the focus-point strip [67–70] that is allowed by all the above constraints, where the LSP is mainly Higgsino-like with a mass ~ 1000–1100 GeV. However, there are some cases in which a lower neutralino mass $\gtrsim 450$ GeV may be allowed,

and other cases with an allowed strip at masses $\gtrsim 1200$ GeV. In all these cases the spin-independent dark matter scattering cross section may be within reach of upcoming experiments. On the other hand, when $A_0 = 3m_0$ only LSP masses $\gtrsim 6$ TeV are allowed, for which the dark matter scattering cross section is well below the neutrino "floor" [71–73]. Section 6 discusses the case when $A_0 = 3\,m_0$ and $\mu > 0$, when there is a single dark matter strip where stop coannihilation is dominant, the uncertainty in the m_h calculation is greater, and dark matter interactions are well below the experimental limits. We find that when $\tan\beta \gtrsim 20$ the portion of the stop coannihilation strip that is allowed by m_h within the calculational uncertainty extends from high masses down to the range of stop masses excluded by LHC searches. Finally, Sect. 7 discusses the relatively simple case when $A_0 = 0$ and $\mu < 0$, and Sect. 8 summarizes our conclusions.

2 Dark matter strips in the CMSSM parameter space

We first summarize the essential features of the CMSSM that are relevant for our study. As usual, the assumption of universality for each of the various classes of soft supersymmetry-breaking parameters at the scale $\sim 10^{16}$ GeV where the SM couplings unify leaves us with the following 4 continuous parameters: the scalar mass, m_0, the gaugino mass, $m_{1/2}$, the trilinear soft supersymmetry-breaking parameter, A_0, and the ratio of supersymmetric Higgs vev's, $\tan\beta$. In addition there is the unknown sign of the Higgsino mixing parameter, μ, which we take to be positive in this section. Historically, this choice has been motivated by the sign of the difference between the SM calculation of $g_\mu - 2$ [74–80] and its experimental value [81–83]. However, this choice can now be questioned on two grounds. One is that the supersymmetric contribution to $g_\mu - 2$ is negligible for the relatively large supersymmetry-breaking scales found in our CMSSM analysis [84–100], and the other is that recent lattice calculations [101] cast doubt on the magnitude of the significance between the SM calculation of $g_\mu - 2$ and its experimental value. Accordingly, we also comment on the status of the CMSSM for negative μ in Sect. 7.

The high precision of the determination of the cold dark matter density by *Planck* and other experiments [26] constrains the parameters of any supersymmetric model to thin hypersurfaces in parameter space, which appear as narrow strips in any planar slice through parameter space. Along these strips, a single mechanism usually controls the dynamics of freeze-out, and obtaining the appropriate density generally requires some specific mixing or relationship between the masses of the sparticles controlling this mechanism. When the LSP mass is relatively large, as suggested by the non-detection of sparticles at the LHC [17–20] and value of m_h [29–31], sometimes more than one mechanism plays a

role. These relationships frequently take the form of a near-degeneracy between the masses of the LSP and the next-to-lightest supersymmetric particle (NLSP), so as to suppress the LSP density via coannihilation [15,102–124], a direct-channel resonance with mass $\sim 2m_{\text{LSP}}$ [1,125–128], or some other specific mass spectrum as in the focus-point region [67–70].

In this section, we have imposed $A_0 = 0$. Generally, one might expect that the A-terms are comparable in magnitude to the other soft supersymmetry-breaking parameters, $m_{1/2}$ and m_0, at the GUT scale.[1] As we see below, large values of A_0 tend to increase the calculated Higgs mass, and thus would require a somewhat less massive supersymmetry spectrum. While one can motivate A_0 from, e.g., anomaly mediation [129–134], our primary motivation lies in studying the CMSSM focus-point region, which contains much of the phenomenologically viable parameter space but disappears when $A_0 \gtrsim m_0$.

The principal dark matter strips in the CMSSM are those where the focus-point mechanism [67–70] is operative, or where stop [15,112–119,124] and/or neutralino/chargino coannihilation [120–124] is dominant, or where resonant exchanges of the neutral heavy Higgs bosons H/A in the s-channel [1,125–128] suppress the relic LSP density. In some parameter planes there are also important regions of the dark matter strips where a single mechanism is insufficient to lower the relic density to its cosmological value, but this is made possible by combinations of these mechanisms that are in play simultaneously.

The panels of Fig. 1 display the results of performing a Markov chain Monte Carlo (MCMC) scan of $m_{1/2}, m_0$ parameter space with $A_0 = 0$ and $\mu > 0$ for the indicated fixed values of $\tan\beta$. The MCMC scan determines the coordinates $(m_{1/2}, m_0)$ for which $\Omega_\chi h^2 = 0.12 \pm 0.0036$, which is the 3σ range as determined by *Planck* [26]. The MCMC code we run employs mainly a Metropolis-Hastings algorithm [135,136]. The basic criterion we use to run the MCMC code is to find points in the parameter space that are compatible with the *Planck* 3σ range for $\Omega_\chi h^2$. This is an efficient way to delineate the dark matter strips in the parameter space. We stress that the MCMC method we employ does carry any statistical weight, but is merely a scanning code. Some of the gaps seen in the strips are due to incompleteness of the scanning process.

Information on the mechanism (or mechanisms) responsible for sufficient annihilation prior to freeze-out is coded by the color of the point. Black points lie along the focus-point strip where $\mu \sim 1$ TeV and the LSP is predominantly a Higgsino of mass 1.1 TeV. At slightly larger values of m_0

---

[1] At low energies, due to the RGE running of all of the mass terms, the A-terms are of the same order as the other supersymmetry-breaking masses.
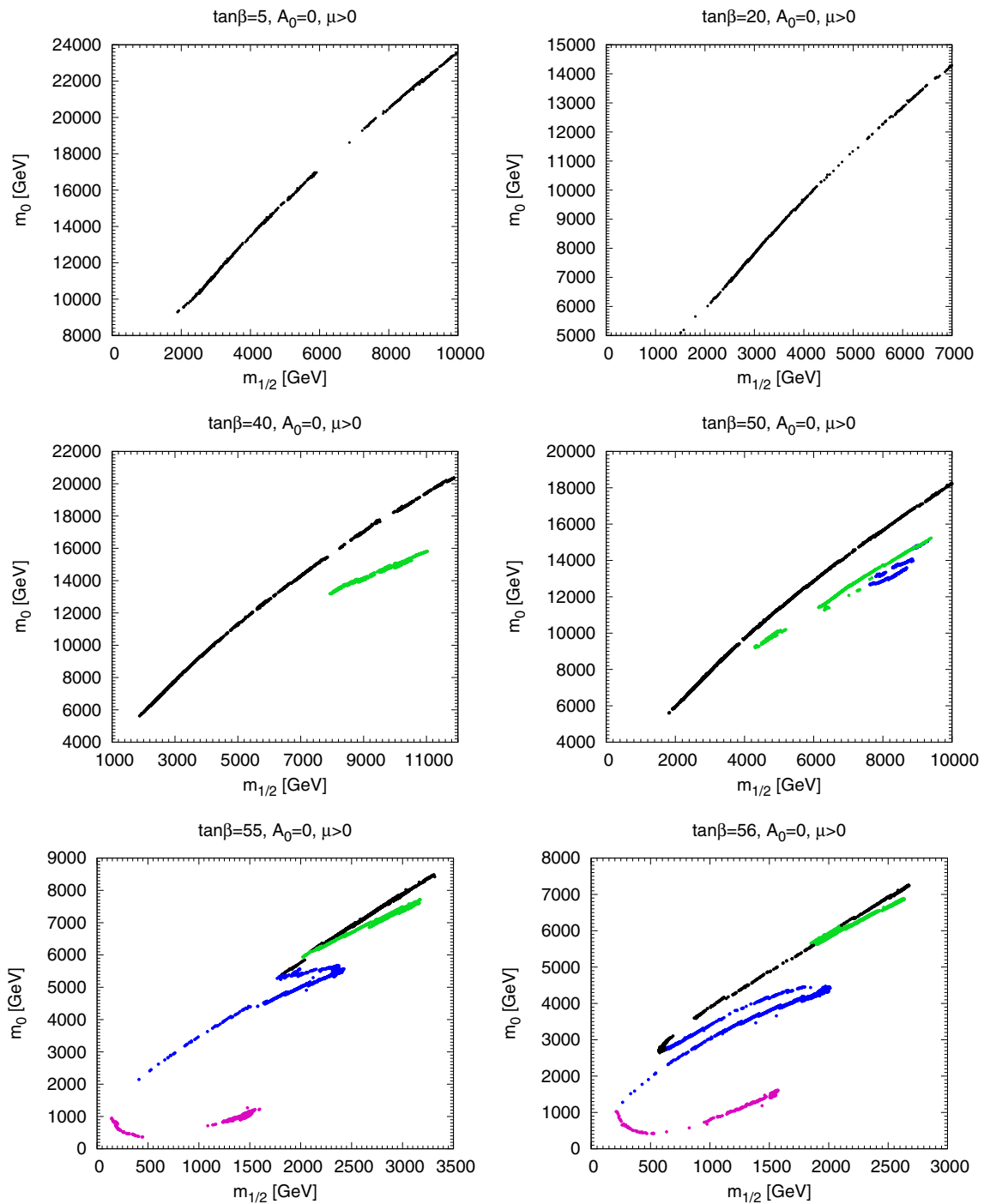
Fig. 1 The dark matter strips for $\tan \beta = 5$, 20, 40, 50, 55 and 56, all assuming $A_0 = 0$ and $\mu > 0$

for each point on this strip, μ^2 is driven to negative values and radiative electroweak symmetry breaking is no longer possible. Below the strip, the LSP is predominantly a bino, with some exceptions noted below. In some cases, at values of m_0 below the focus-point region the bino LSP acquires non-negligible Higgsino components, in which case the neu-

tralino becomes 'well-tempered' [137,138]. These points are coloured green.

The purple points at lower m_0 and large $\tan \beta$ lie along the funnel where the LSP mass is close to half the heavy Higgs masses and the dominant dark matter mechanism is rapid LSP annihilation via these s-channel resonances. However, as $m_{1/2}$ increases, this s-channel annihilation is suppressed

by the heavy Higgs widths and the annihilation cross section is insufficient to reduce the relic density to the required value, which is why the purple points terminate at an endpoint. At larger m_0, in addition to s-channel Higgs pole contributions, the LSP becomes well-tempered and the combination of these contributions leads to a low relic density. These points are colored blue. Coannihilations of the bino-like state, the two Higgsinos and chargino also play a role in determining the final relic density. In addition, as we will see, there is level crossing between the neutralino states in some areas of parameter space. Here the neutralino may be well-tempered and coannihilations may also be important. These points will be colored green. We describe in the following how each of these possibilities arises for different values of $\tan \beta$.

The top left panel of Fig. 1 shows the $(m_{1/2}, m_0)$ plane for $\tan \beta = 5$, $A_0 = 0$ and $\mu > 0$. It features a single dark matter strip where the focus-point mechanism is operative, which extends beyond the range of $m_{1/2} \leq 10$ TeV that we display. The $(m_{1/2}, m_0)$ plane for $\tan \beta \lesssim 20$, $A_0 = 0$ and $\mu > 0$ is similar, as seen in the top right panel of Fig. 1. This one is truncated at $m_{1/2} = 8$ TeV, because the extensions of this strip to larger $m_{1/2}$ is not compatible with the LHC measurement of m_h, as we see later.

In the $\tan \beta = 40$ case as seen in the middle left panel of Fig. 1, in addition to the black focus point strip, a closely-spaced pair of green strips appears when $m_{1/2} > 7$ TeV. Here, the neutralino (mostly bino) is well-tempered and the non-negligible Higgsino components in the LSP lead to enhanced annihilations that bring the relic density into the allowed range. On either side (higher and lower m_0) of the pair of strips, the relic density is too high, and between the strips the relic density is suppressed. However, as we will see these points are excluded by both m_h and the upper limit on spin-independent dark matter scattering.

As aids to understanding the origins of the strips, we plot slices across the $(m_{1/2}, m_0)$ plane showing the relic density, masses, and neutralino composition as functions of m_0 for fixed values of $m_{1/2}$. As a first example for $\tan \beta = 40$, $A_0 = 0$ and $\mu > 0$, we fix $m_{1/2} = 5$ TeV in the left panels of Fig. 2 and in $m_{1/2} = 9$ TeV in the right panels. The top panels illustrate how the relic density varies with m_0. We see that along both slices the relic density decreases as the boundary of electroweak symmetry breaking is approached when $m_0 \gtrsim 11$ (17) TeV, corresponding to the focus-point strip in the middle left panel of Fig. 1. The dark matter density is generally larger than allowed by *Planck* and other measurements at lower m_0. However, there are dips in the relic density at $m_0 \sim 10$ (14) TeV for $m_{1/2} = 5.0$ (9.0) TeV, including a pair of m_0 values where the *Planck* relic density is found for $m_{1/2} = 9$ TeV. These values lie on the pair of green lines seen in the middle left panel of Fig. 1.

The middle panels of Fig. 2 display the masses of the lightest neutralino, m_{χ_1} (black line), the next two neutralino masses, m_{χ_2} (purple line) and m_{χ_3} (blue line) and half the mass of the pseudoscalar Higgs boson, $m_A/2$ (red line). The three mass eigenstates are either mostly pure or mixed states of the bino and two Higgsinos, as the wino is always heavy and does not enter in the discussion of the parameter ranges discussed here. The bino-like state (whether the LSP or not) has a relatively constant mass, while the two Higgsino masses decrease with increasing m_0 as μ decreases over the displayed range of m_0, as a result of the Higgs potential minimization conditions. Coannihilation is the most important dark matter mechanism when two or more of the neutralinos are close in mass. Comparing the middle and top panels, one sees that the dips in the relic density coincide with the degeneracy in the neutralino masses leading to coannihilation, whereas s-channel annihilation via heavy Higgs poles is less important in this case because m_χ is quite different from $m_A/2$.

The bottom panels of Fig. 2 show that the dips in the relic density at relatively low m_0 are correlated with crossovers in the neutralino mass eigenstates and corresponding variations in the LSP composition, with the LSP acquiring a significant Higgsino component near the crossovers, leading to a well-tempered neutralino. Around this cross-over the lightest eigenstate transitions from a bino-like state with Higgsino components $Z_{13} \simeq 1/2$ and $Z_{14} \simeq -1/2$ to a Higgsino-like state with $Z_{33} \simeq 1/2$ and $Z_{34} \simeq -1/2$ (with $Z_{11} \simeq 1/\sqrt{2}$ in both cases). As one can see, these states are maximally well-tempered. We display the bino component (Z_{11}) and the two Higgsino components (Z_{13} and Z_{14}) of the bino-like state, which is not necessarily the LSP. This state is the LSP for m_0 below the dip. When the LSP eigenstate flips, the Higgsino components of the bino-like state are now $Z_{13} \simeq -1/2$ and $Z_{14} \simeq 1/2$ still with $Z_{11} \simeq 1/\sqrt{2}$. At larger m_0, this state is again mostly a pure bino, though it is no longer the LSP. As seen more clearly in the middle right panel of Fig. 2, the crossover is reflected in a bump in the LSP mass where coannihilation with χ_2 and the lighter chargino is enhanced, suppressing the relic density around the local minimum seen in the top right panel of Fig. 2.[2]

The middle right panel of Fig. 1 shows the $(m_{1/2}, m_0)$ plane for $\tan \beta = 50$, where the focus-point strip (black points) is again supplemented by additional features at lower m_0 that resemble the second feature that appeared for $\tan \beta = 40$, but extend to lower $m_{1/2}$ and exhibit a richer structure. As in the case of $\tan \beta = 40$, there are a pair of strips where the neutralino is well-tempered. These are represented by the green points which extend down to $m_{1/2} \approx 4$ TeV. At larger $m_{1/2}$, an additional pair of strips appear where the LSP is somewhat less well-tempered, but sits near the heavy Higgs

---

[2] In these and subsequent analogous figures we see other glitches in the composition of the LSP and particle masses, and consequently the relic density, which are numerical artifacts.
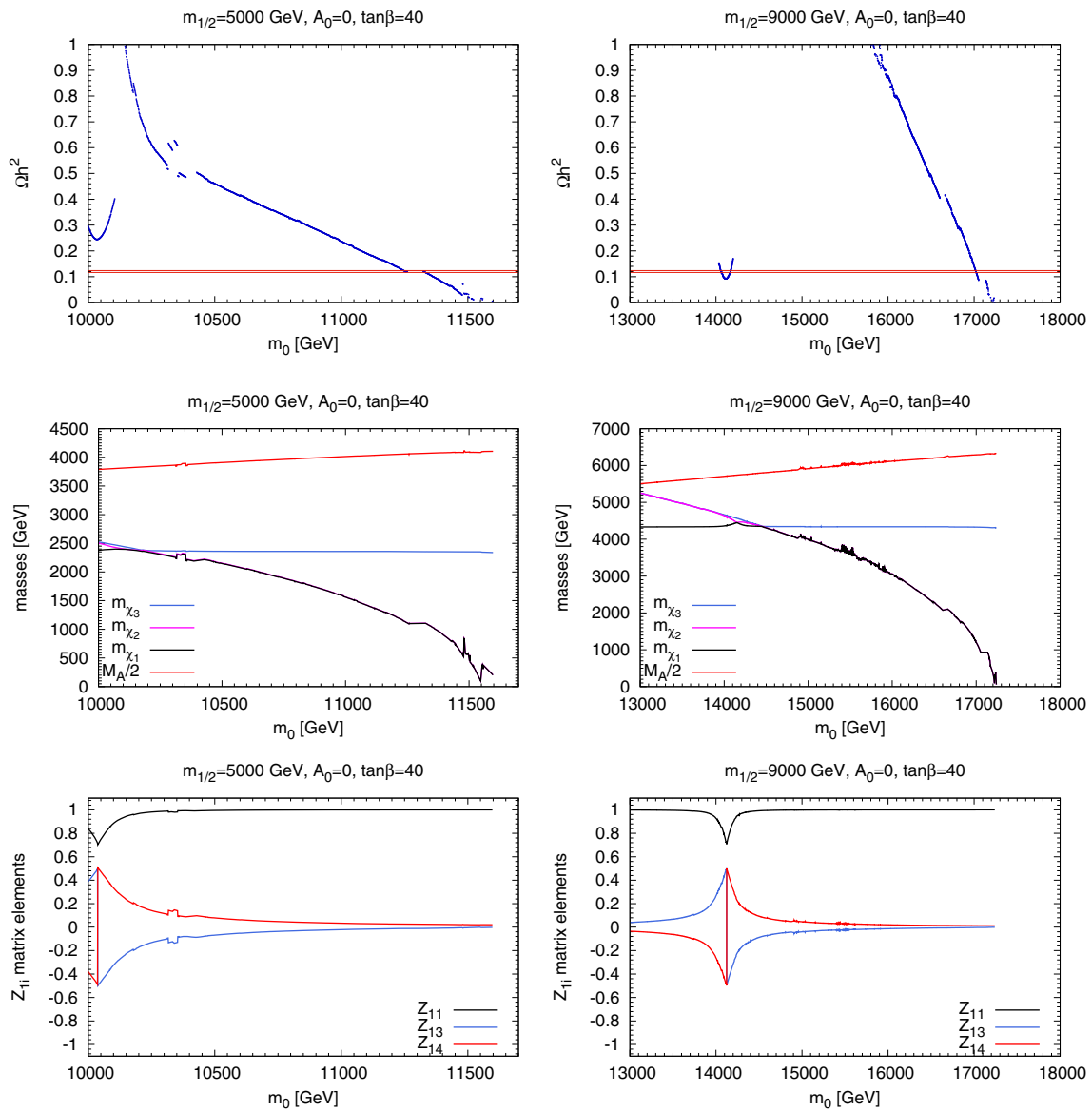
Fig. 2 Cuts across the $(m_{1/2}, m_0)$ planes for $\tan\beta = 40$, $A_0 = 0$ and $\mu > 0$ for varying m_0 and fixed $m_{1/2} = 5.0$ TeV (left panels) and 9.0 TeV (right panels), showing the dark matter density (top panels), particle masses (middle panels) and the composition of the bino-like neutralino (bottom panels)

pole. For these points, it is the combination of the *s*-channel annihilations with the bino-Higgsino mixing contributions that lead to a cross section that is large enough to obtain the correct relic density.

The interplay of different dark matter mechanisms for $\tan\beta = 50$ is illustrated in Fig. 3, where m_0 varies along slices across the $(m_{1/2}, m_0)$ plane at fixed $m_{1/2} = 5$ TeV (left panels) and 7.8 TeV (right panels). We see in the top left panel that the *Planck* value of the relic density is attained for three values of m_0.[3] These correspond to the focus-point

strip at $m_0 \approx 11.3$ TeV and a pair of values of m_0 around 10 TeV. The latter correspond to the green strips seen in Fig. 1 where the well-tempered nature of the LSP is sufficient for reducing the relic density into the cosmological range. In contrast, at higher $m_{1/2}$, as seen in the right panels, there are five values of m_0 where the desired relic density is attained. Once again the highest value at $m_0 \approx 15.4$ TeV corresponds to the focus-point strip. The cluster of points around $m_0 \simeq 13$ TeV contains 4 values of m_0 where the

---

[3] There are also a handful of points seen at $m_0 \approx 9.3$ TeV. These points are almost exactly on a coannihilation pole where $(m_{\chi_1} + m_{\chi_2})/m_H -$

Footnote 3 continued

$1 < 10^{-6}$, where H is the heavy Higgs scalar. We do not discuss these points further.
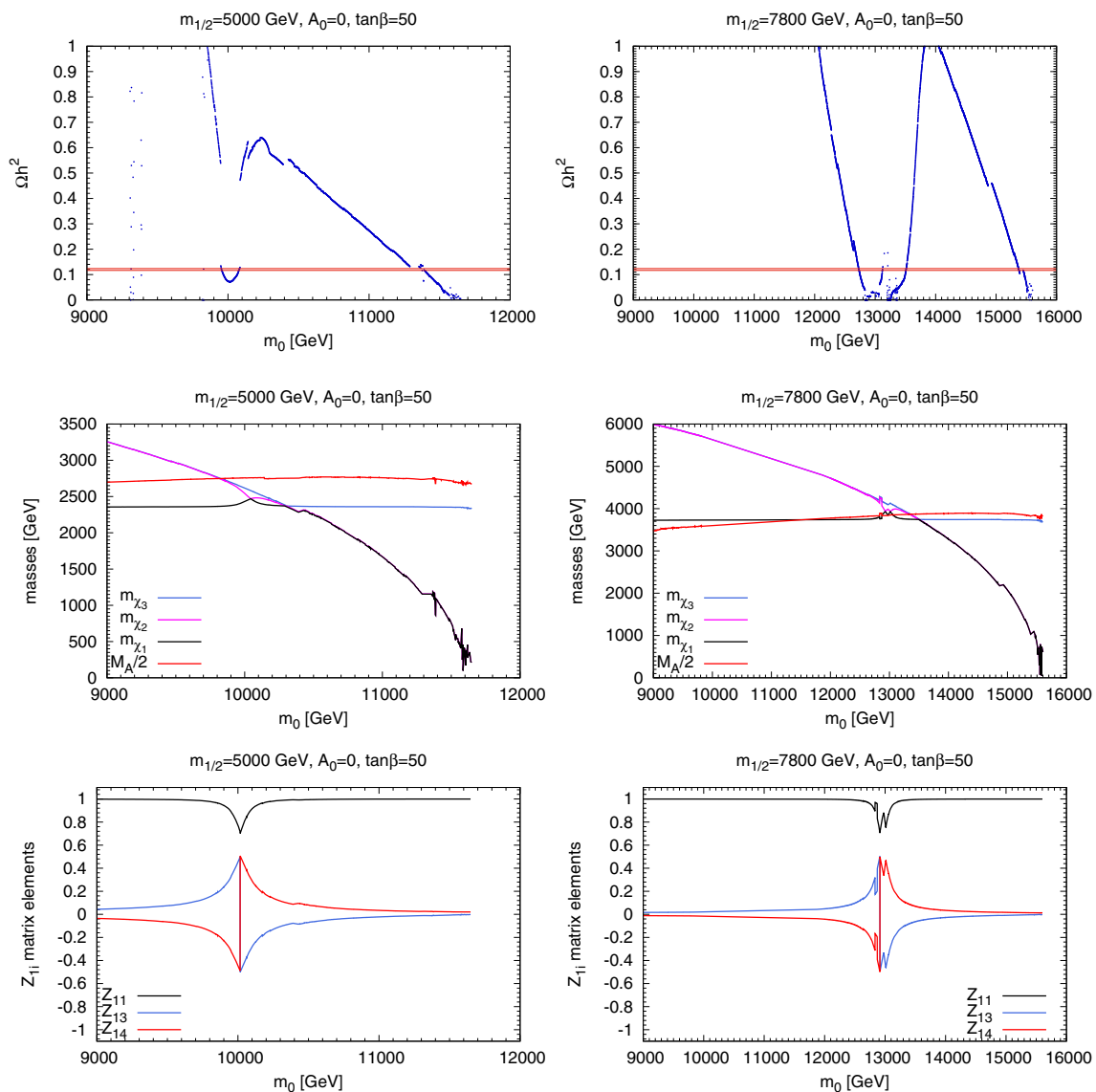
Fig. 3 Cuts across the $(m_{1/2}, m_0)$ planes for $\tan\beta = 50$, $A_0 = 0$ and $\mu > 0$ for varying m_0 and fixed $m_{1/2} = 5$ TeV (left panels) and 7.8 TeV (right panels), showing the dark matter density (top panels), particle masses (middle panels) and the composition of the LSP (bottom panels)

cosmological value $\Omega h^2 = 0.12$ is crossed. These 4 values arise from the interplay of rapid s-channel annihilation via the A/H resonances (which is most important where the red and black lines cross in the middle panels, which does not occur for $\tan\beta = 40$) and LSP coannihilation with the Higgsinos and lighter chargino (which is most important where the blue and black lines approach each other in the lower panels). Within this cluster of points, those with lower m_0 require both s-channel annihilations and a well-tempered neutralino, whereas at higher m_0, the neutralino level crossing is also sufficient to suppress the relic density. These correspond to the blue and green strips seen in Fig. 1. At higher m_0, the Higgsino becomes the LSP, and the annihilation cross section enhancements disappear until m_0 is sufficiently large that

$m_\chi \approx \mu \approx 1.1$ TeV, and the relic density falls back to 0.12 due to neutralino/chargino coannihilations among the Higgsinos. Finally, the boundary of the electroweak symmetry breaking region is reached when $m_0 \approx 15.5$ TeV.

The $(m_{1/2}, m_0)$ plane for $\tan\beta = 55$ shown in the bottom left panel of Fig. 1 exhibits additional features. We note that the focus-point strip terminates because the renormalization-group running of the top Yukawa coupling diverges at larger $m_{1/2}$. The purple strip corresponds to a funnel region starting at low m_0 where s-channel annihilation through the heavy Higgs bosons dominates. This terminates at about $m_{1/2} \sim 1.6$ TeV when, due to the increasing heavy-Higgs width, the annihilation cross section becomes too small to reduce the relic density into the range allowed by *Planck* and

other measurements. In the region above and to the right of this funnel, the relic density is too high. For fixed $m_{1/2}$, e.g., $m_{1/2} = 2$ TeV, as m_0 is increased, the heavy Higgs masses increase and $2m_\chi < m_A$, until at still higher m_0, μ begins to decrease. This has the effect of decreasing m_A and moving the LSP back on the Higgs pole, lowering the Higgsino/chargino masses and increasing the Higgsino component of the LSP. This results in the pair of blue strips that form a second funnel region, where the annihilation cross section is augmented by an increasing neutralino coannihilation contribution sufficiently to lower the relic density to an acceptable value. Further increasing m_0 moves the LSP off the pole and the relic density is again too big until m_0 is sufficiently large that μ has dropped enough for the LSP to become mostly Higgsino and the focus-point strip is reached. At higher $m_{1/2}$, e.g., $m_{1/2} = 2.8$ TeV, the funnel is not able to bring the relic density sufficiently low, even though enhanced by coannihilation. However, at larger $m_0 \sim 7$ TeV a large Higgsino component in the LSP increases the cross section producing the green pair of strips below the black focus-point strip.

Figure 4 shows slices through the $(m_{1/2}, m_0)$ plane for $\tan\beta = 55$ with $m_{1/2} = 2$ TeV (left panels) and 2.8 TeV (right panels). As we see in the top panels, for both values of $m_{1/2}$ the relic density exceeds the *Planck* range at low m_0, namely for $m_0 < 5000$ and 7000 GeV, respectively. For $m_{1/2} = 2000$ GeV, when $m_0 < 1.22$ TeV, the lighter stau is the LSP. At higher m_0, the bino becomes the LSP and its mass is close to half the heavy Higgs mass, but it is past the endpoint of the funnel region and, although the relic density is low, it is still above the range allowed by cosmology.[4] At slightly higher m_0, $m_{A/H}$ drops, LSP annihilation via the heavy Higgs poles is suppressed and the relic density is high. However, as one sees in the middle left panel of Fig. 4, $m_{H/A}$ rises, LSP annihilation via the heavy Higgs poles becomes possible, and the relic density decreases leading to the dip seen in the upper left panel at $m_0 \sim 2$ TeV. However, it does not fall sufficiently before the LSP mass moves away from half the pole mass, and begins to rise for $m_0 \gtrsim 2$ TeV. At $m_0 \gtrsim 4$ TeV, μ and the Higgsino masses begin to drop. The Higgs pseudoscalar mass also drops and heavy-Higgs pole annihilation becomes possible again, though this time with an increased Higgsino component and a smaller mass splitting with the chargino. Then, at $m_0 \approx 5$ TeV the relic density is sufficiently low to become compatible with *Planck* and other data. The "valley" around 5200 GeV is characteristic of s-channel annihilation via the A/H bosons and explains the funnel-like feature of the blue strips in the bottom left

panel of Fig. 1. As seen there, this strip terminates when $m_{1/2} \sim 2400$ GeV. Above $m_0 \simeq 5.2$ TeV, the LSP moves off the pole again and the relic density begins to rise again until $m_0 \approx 5.7$ TeV, where the Higgsino becomes the LSP and the focus-point strip is encountered.

Similar behaviour is seen in the right panels of Fig. 4 for $m_{1/2} = 2.8$ TeV. While the relic density shows a minimum around $m_0 \approx 5.5$ TeV, we see that the funnel alone is not sufficient in obtain the *Planck* value for relic density. As the LSP moves off the pole at higher m_0, the relic density begins to rise until the Higgsino component of the LSP increases sufficiently to raise the cross section and hence reduce the relic density. The relic density hits a local minimum and then rises as the LSP becomes a pure Higgsino, subsequently falling through the *Planck* value when the Higgsino mass falls to ~ 1 TeV.

All these features are present also in the bottom right panel of Fig. 1, which displays the corresponding $(m_{1/2}, m_0)$ plane for $\tan\beta = 56$. As for $\tan\beta = 55$, the focus-point strip terminates because the renormalization-group running of the top Yukawa coupling diverges at larger $m_{1/2}$.
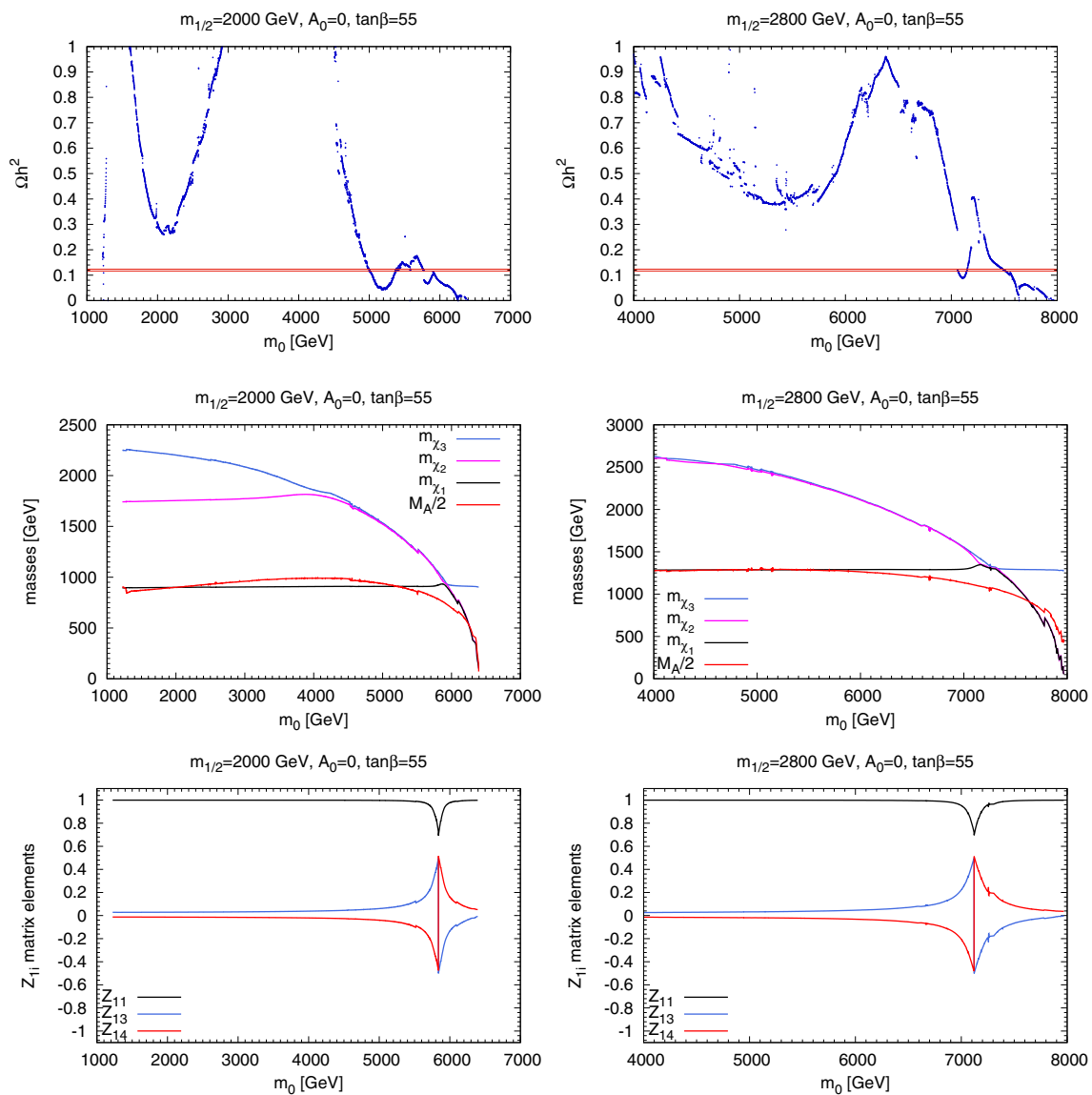
Figure 5 shows slices across the $(m_{1/2}, m_0)$ plane for $\tan\beta = 56$ for the fixed values of $m_{1/2} = 950$ (upper panels) and 2500 GeV (lower panels). In the first case we see clearly that the *Planck* value of the relic density is attained at four different values of m_0, corresponding to the funnel, two strips corresponding to the coannihilation/funnel combination and finally the focus-point region. In the left panel we see again that the LSP is near the heavy-Higgs pole at both low and high m_0. On the other hand, for $m_{1/2} = 2500$ GeV (right panels of Fig. 5) we see that the *Planck* density is attained only for two very similar values of $m_0 \gtrsim 6700$ GeV that are in well-tempered region and at higher $m_0 \sim 6900$ GeV when the focus point strip is reached.

3 LHC constraints

3.1 Sparticle searches

The headline sparticle searches at the LHC are those for squarks and gluinos, both of which are sensitive to masses $\lesssim 2$ TeV in simplified models, e.g., assuming that some specific decay mode has a branching ratio of 100% and the LSP mass is negligible. The squark limit would correspond to $m_0 \gtrsim 2$ TeV for small $m_{1/2}$, and the gluino limit would correspond to $m_{1/2} \gtrsim 800$ GeV. These constraints do not impinge on the $A_0 = 0$ regions of interest in Fig. 1. Indeed the mass spectrum we find is quite heavy. In Fig. 6, we show the lighter stop mass as a function of $m_{1/2}$ along the dark matter strips. As one can see, the stop masses are similar to (though slightly smaller than) m_0. Similarly in Fig. 7, we show the gluino mass along the strips. The gluino mass is typically

---

[4] An exception is presented by a handful of points where the relic density is suppressed at $m_{1/2} \simeq 1.23$ TeV where LSP coannihilations with the lighter stau are important and the stau mass is very close to one half of the heavy Higgs mass, leading to enhanced s-channel stau annihilations.

Fig. 4 Cuts across the $(m_{1/2}, m_0)$ planes for $\tan \beta = 55$, $A_0 = 0$ and $\mu > 0$ for varying m_0 and fixed $m_{1/2} = 2.0$ TeV (left panels) and 2.8 TeV (right panels), showing the dark matter density (top panels), particle masses (middle panels) and the composition of the LSP (bottom panels)

$\simeq 2 - 3m_{1/2}$. On the other hand, as we discuss in Sect. 6, for $A_0 = 3\,m_0$ searches for light stops with a compressed spectrum exclude masses just below the region of the stop coannihilation strip allowed by the FeynHiggs 2.18.1 calculation of m_h at the 1-σ level. The stop masses in this case are nearly degenerate with the LSP mass. The gluino mass is again roughly $2 - 3m_{1/2}$.

3.2 Higgs mass constraint

The world average of the Higgs boson mass is 125.25 ± 0.17 GeV [139]. In order to calculate m_h in the CMSSM we use the FeynHiggs 2.18.1 code [32], which returns an uncertainty estimate Δm_h as well as the best estimate of m_h

for each choice of model parameters. The uncertainty estimate is quite variable being, e.g., significantly smaller for $A_0 = 0$ than for $A_0 = 3\,m_0$. Conservatively, for $A_0 = 0$ we assume that $\Delta m_h = 1.5$ GeV, which corresponds to somewhat more than twice the typical numerical estimate of Δm_h, commenting in passing on the prospective implications for $\Delta m_h \sim 0.5$ GeV. On the other hand, the typical FeynHiggs 2.18.1 uncertainty estimate for $A_0 = 3\,m_0$ is much larger, $\Delta m_h \gtrsim 3$ GeV (and $\tan \beta$ dependent), which does not exclude any portions of the stop coannihilation strips for $A_0 = 3\,m_0$.

The panels in Fig. 8 illustrate how the m_h constraint restricts the allowed ranges of the dark matter strips for $\tan \beta = 5, 20, 40, 50, 55$ and 56 when $A_0 = 0$ and $\mu > 0$.
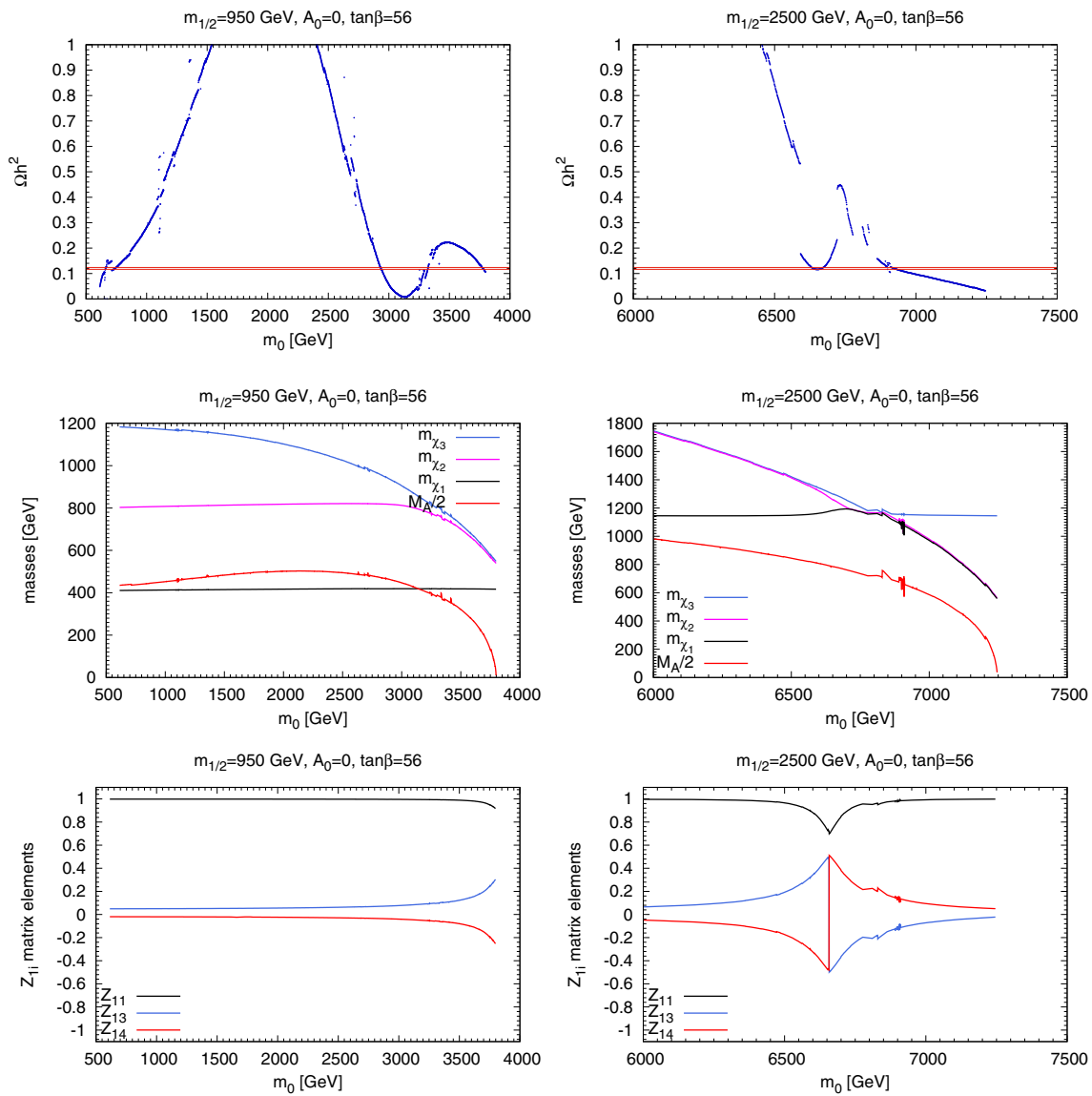
Fig. 5 Cuts across the $(m_{1/2}, m_0)$ planes for $\tan\beta = 56$, $A_0 = 0$ and $\mu > 0$ for varying m_0 and fixed $m_{1/2} = 950$ GeV (left panels) and 2.5 TeV (right panels), showing the dark matter density (top panels), particle masses (middle panels) and the composition of the LSP (bottom panels)

For $\tan\beta = 5$ (top left panel), $m_{1/2} \gtrsim 7$ TeV is allowed for $\Delta m_h = 1.5$ GeV, but only a limited range of $m_{1/2} \gtrsim 9$ TeV if we assume $\Delta m_h \simeq 0.5$ GeV. (Note that the focus-point strip continues to larger values of $m_{1/2}$ than those displayed. The apparent endpoint is due to the finite range of our MCMC scan.) For $\tan\beta = 20$ (top right panel), the range 2.4 TeV $\lesssim m_{1/2} \lesssim 6.6$ TeV is allowed for $\Delta m_h = 1.5$ GeV, whereas only the range 3.6 TeV $\lesssim m_{1/2} \lesssim 5$ TeV would be favoured for $\Delta m_h \simeq 0.5$ GeV. Similar ranges of $m_{1/2}$ are allowed (favoured) for $\tan\beta = 40$, as seen in the middle left panel of Fig. 8. We see now that the well-tempered (green) strips at $m_{1/2} > 8$ TeV are excluded as the calculated Higgs mass is too large even when conservative allowance is made for the uncertainty in the calculation.

When $\tan\beta = 50$ (middle right panel), a portion of the well-tempered strip is allowed, extending to $m_{1/2} \simeq 7$ TeV for $\Delta m_h = 1.5$ GeV. However, the additional strips at large $m_{1/2}$ where s-channel annihilations contribute (blue points) lead to values of m_h that are too large. When $\tan\beta = 55$ (bottom left panel of Fig. 8), only a portion of the focus-point strip with $m_{1/2} \gtrsim 2.5$ TeV is allowed for $\Delta m_h = 1.5$ GeV, increasing to $m_{1/2} \gtrsim 3$ TeV for $\Delta m_h \simeq 0.5$ GeV. We see also that parts of the coannihilation/well-tempered (green) strips for $\tan\beta = 55$ also fall within the experimental range for the Higgs mass. In contrast, in the funnel/coannihilation/well-tempered strips (blue) the Higgs mass is always too small, as it is in the funnel region (purple). Finally, we see that for $\tan\beta = 56$ (bottom right panel) the correct value of m_h is
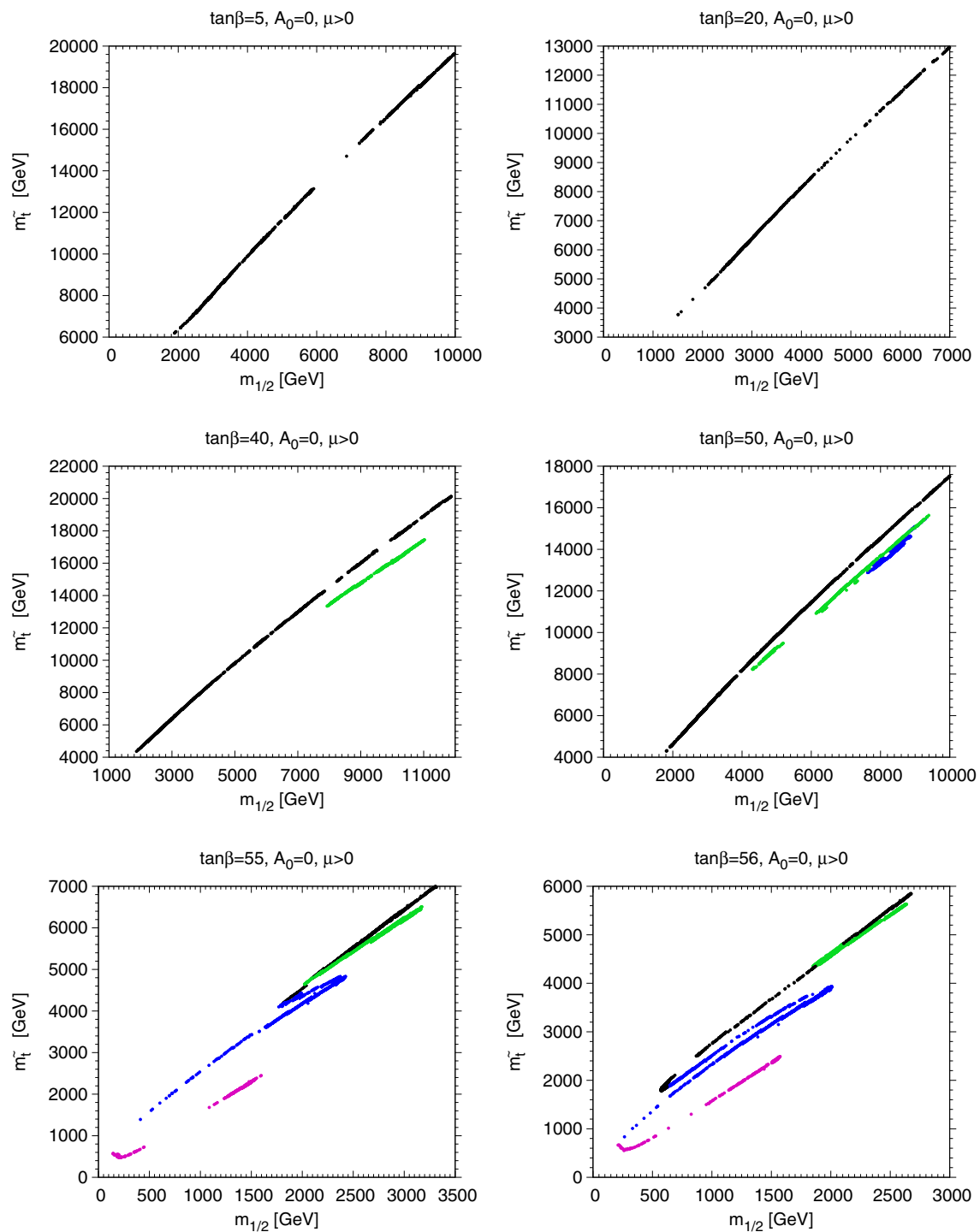
Fig. 6 The lighter stop mass along the dark matter strips for $\tan\beta = 5, 20, 40, 50, 55$ and 56, with $A_0 = 0$ and $\mu > 0$

only attained when $m_{1/2} \gtrsim 2.5$ TeV at the tip of the black and green strips.[5]

---

[5] We recall that these strips cannot be extended for this value of $\tan\beta$ because of the divergence of the Yukawa couplings during renormalization group evolution.

## 4 Constraints on dark matter interactions

4.1 Spin-independent dark matter scattering

Many experiments have used massive nuclear targets to probe coherent spin-independent LSP-nucleon scattering. The most
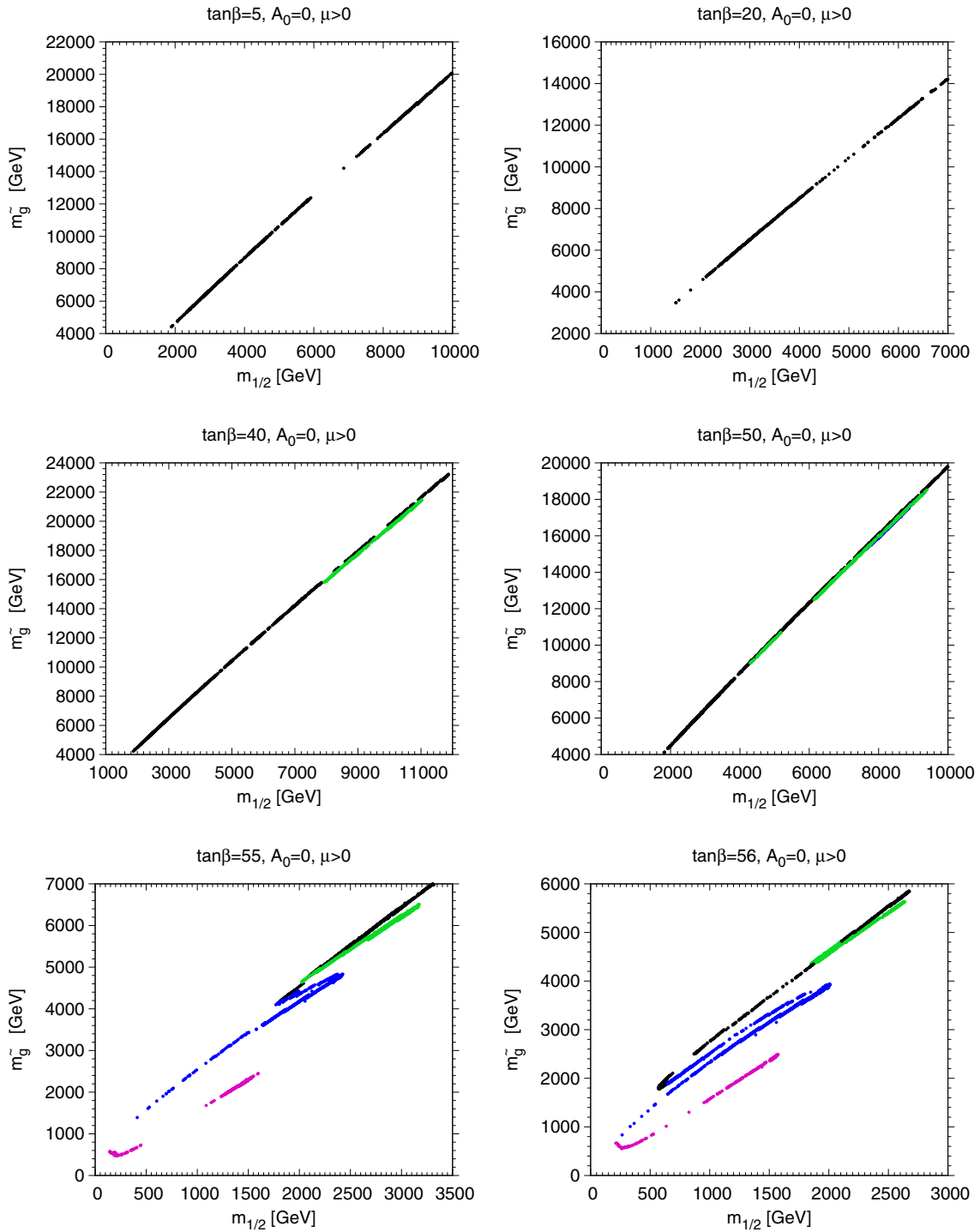
Fig. 7 The gluino mass along the dark matter strips for $\tan\beta = 5, 20, 40, 50, 55$ and 56, with $A_0 = 0$ and $\mu > 0$

recent such experiment is LUX-ZEPLIN (LZ) [25], which uses a xenon target to establish a stronger upper limit on the spin-independent LSP-nucleon scattering cross section than the previous XENON1T [21], PandaX-4T [23,24], LUX [22] and DEAP-3600 [140] experiments.

The computation of the spin-independent cross section that we use was described in detail in [141,142]. As is well known, the spin-independent cross section is very sensitive to the quark matrix elements, $\langle N|\bar{q}q|N\rangle$. These can be expressed in terms of σ terms, notably the $\pi - N\ \sigma$ term $\Sigma_{\pi N}$ and σ_s (see [141,142] for more detail). Here we have used
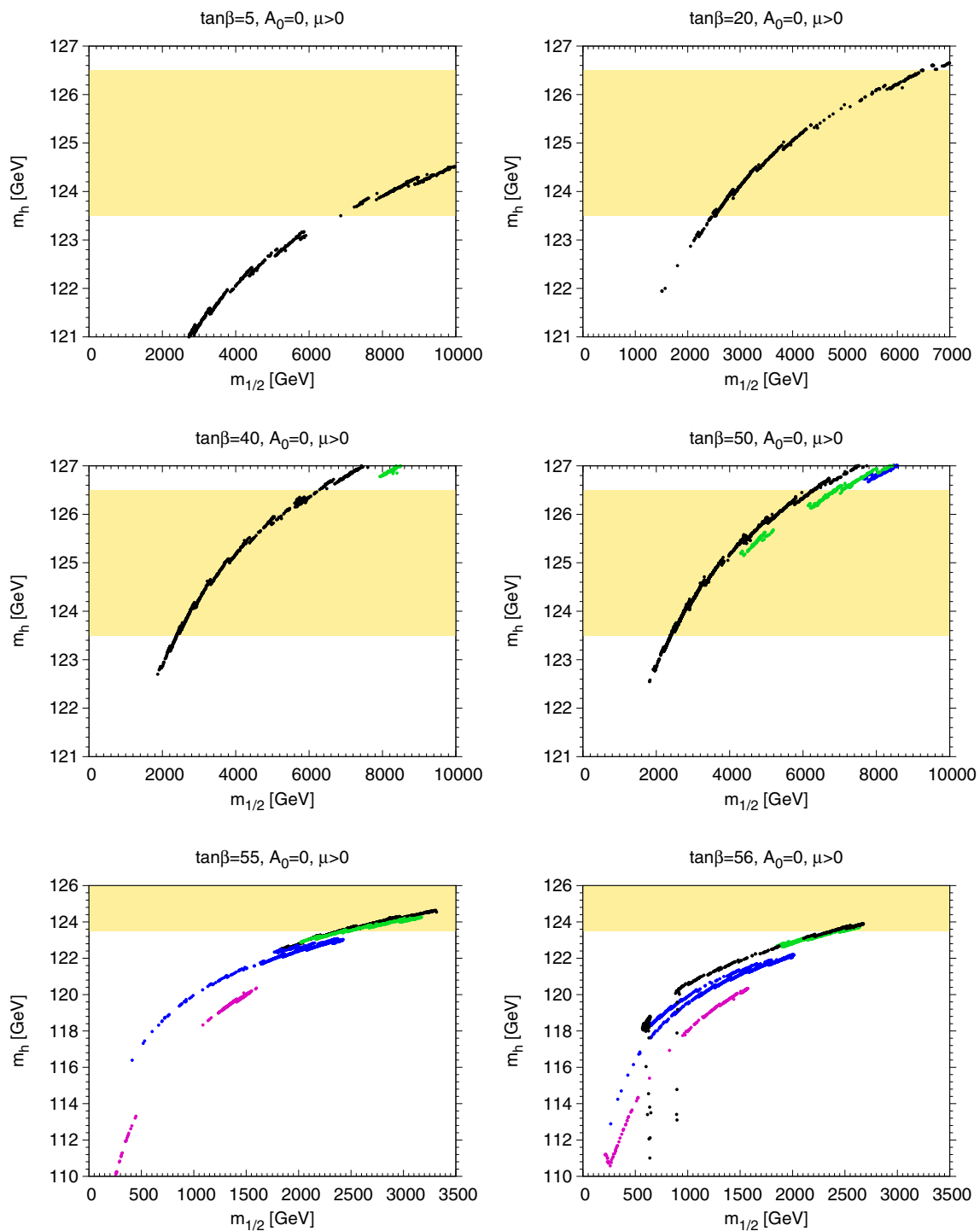
Fig. 8 The yellow shading indicates the impacts of the LHC measurement of m_h, as calculated using `FeynHiggs 2.18.1` and allowing an uncertainty of 1.5 GeV, on the dark matter strips for $\tan\beta = 5, 20, 40, 50, 55$ and 56 with $A_0 = 0$ and $\mu > 0$

$\Sigma_{\pi N} = 46 \pm 11$ MeV and $\sigma_s = 35 \pm 16$ MeV, respectively. The corresponding typical uncertainties in the elastic cross sections are of order 10–15%.

We see in the top and middle panels of Fig. 9 that the spin-independent LSP-nucleon scattering constraint allows

limited regions of the dark matter focus-point strips where $m_\chi \sim 1.0 - 1.1$ TeV for $\tan\beta = 5, 20, 40$ and 50. Along the near vertical strips shown here, although $m_{1/2}$ (and m_0) changes, the LSP mass is nearly constant. For $\tan\beta = 40$, we see that the direct detection experiments are (like the

Higgs mass constraint) able to exclude the well-tempered LSP points (green). We also see in the middle right panel of Fig. 9 that only a small fraction of the well-tempered and funnel points (green and blue) with larger values of m_χ are allowed. We see in the bottom panels of Fig. 9 for $\tan\beta = 55$ and 56 that points along the focus-point strips and in the well-tempered regions (green) are excluded, and only a small fraction of well-tempered/funnel points (blue) are still allowed. These points have $m_\chi \lesssim 1$ TeV and, as we have discussed previously, correspond to Higgs masses that are unacceptably small. Some ranges of the funnel strips (purple) are also still allowed by the spin-independent dark matter scattering constraint, and have also shifted to lower values of $m_\chi \lesssim 800$ GeV. However, these points also correspond to unacceptably low Higgs masses.

These figures show the strong impact of the spin-independent scattering limits when A_0 and $\mu > 0$ and illustrate their potential for even more stringent constraints in the future as their sensitivities reach down towards the neutrino 'floor' [71–73]. We find spin-independent scattering cross sections that lie above the 'floor' for all values of $\tan\beta$ when $A_0 = 0$, for both signs of μ.

4.2 Spin-dependent dark matter scattering

Spin-dependent LSP-nucleon scattering on a nucleus is not coherent, but is proportional to the nuclear spin, which is mainly carried by an odd nucleon. The LZ experiment also set new upper limits on spin-dependent LSP scattering on both the neutron and the proton. The LZ limit on spin-dependent LSP-neutron scattering exploits the fact that two common xenon isotopes have non-zero nuclear spins that are carried mainly by unpaired neutrons: ^{129}Xe (abundance 26.4%, spin 1/2) and ^{131}Xe (21.2% abundance, spin 3/2). The LZ limit on spin-dependent LSP-proton scattering exploits configuration mixing between proton and neutron spin states in these isotopes, but has larger uncertainties and is significantly weaker than their limit on spin-dependent LSP-neutron scattering.[6] The spin-dependent LSP-neutron and -proton scattering cross sections are calculated to be quite similar, so we use here only the LZ limit on spin-dependent LSP-neutron scattering, which provides the most stringent constraint on spin-dependent LSP-nucleon scattering.

We see in Fig. 10 that all the dark matter strips for $\tan\beta \leq 50$ are compatible with the spin-dependent scattering constraint from the LZ experiment. However, there are regions of the funnel strips (purple) for $\tan\beta = 55$ and 56 with $m_\chi \lesssim 100$ GeV that are excluded by this constraint, as seen in the bottom panels of Fig. 10. We note in addition that

there are some well-tempered/funnel points (blue) with LSP masses ~ 200 GeV that are marginally excluded by the LZ spin-dependent scattering constraint.

4.3 Indirect constraints

A variety of products of LSP annihilations may offer detectable signals, including γ rays, neutrinos, positrons, antiprotons and light antinuclei. We consider in this paper γ rays and neutrinos, whose production is relatively straightforward to model and may provide interesting observational constraints. Since annihilation rates are proportional to the square of the local DM density, we study regions where the DM accumulates. These include dwarf spheroidal satellite galaxies (dSphs) [45–50,144–148] and the Galactic Center (GC) [52–55,149], which are potential sources of observable γ fluxes, and the Sun, which is an interesting potential source of energetic neutrinos [64–66,150–152].

4.3.1 Limits on γ fluxes from dwarf spheroidal satellite galaxies

We first examine dSphs as possible sources of γ rays from DM annihilations in the framework of the CMSSM, before revisiting the possible GC constraint on DM annihilations.

The annihilation of neutralinos can yield monochromatic photons via the one-loop processes $\chi\chi \to \gamma\gamma$ and $\chi\chi \to \gamma Z$, and also a continuous spectrum of photons via the decays of π^0s and other hadrons produced by the fragmentation and hadronization of primary annihilation products. The integrated γ-ray signal flux, ϕ_s (typically measured in photons/cm^2/s), expected from the annihilations of DM particles with a density distribution $\rho_{DM}(r)$ is
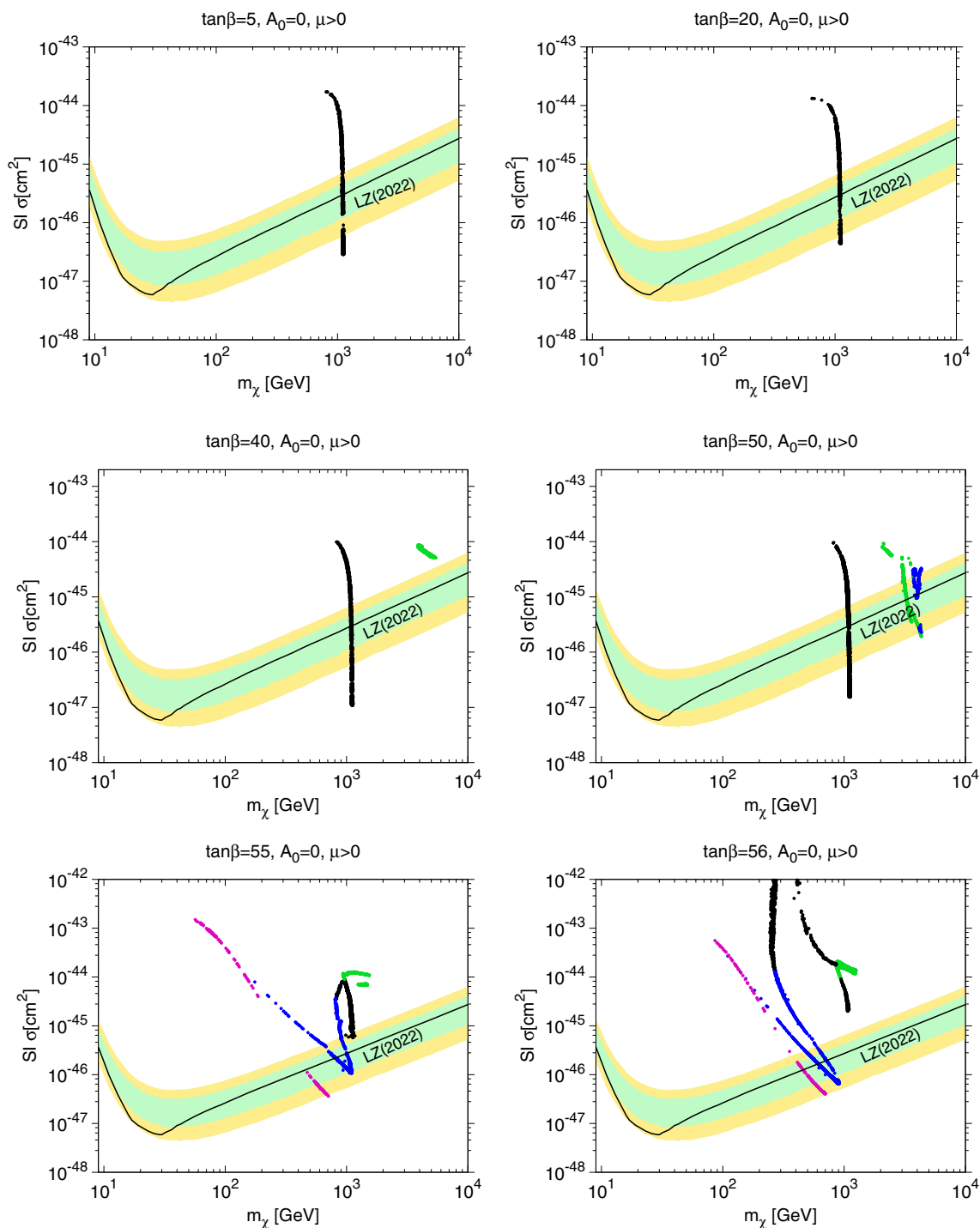
$$\phi_s(\Delta\Omega) = \underbrace{\frac{1}{4\pi}\frac{\langle\sigma\upsilon\rangle}{2m_{DM}^2}\int_{E_{min}}^{E_{max}}\frac{dN_\gamma}{dE_\gamma}dE_\gamma}_{\Phi_{PP}} \times \underbrace{\int_{\Delta\Omega}\int_{l.o.s.}\rho_{DM}^2(r)dld\Omega'}_{\text{J factor}},$$

(1)

whose components we analyze in the following.

The first term of (1), Φ_{PP}, depends on the particle physics properties. In particular, this term is dependent on the thermal annihilation cross section $\langle\sigma\upsilon\rangle$, the mass of the dark matter particle, m_{DM}, and the differential γ ray yield per annihilation, dN_γ/dE_γ, integrated over the experimental energy range. The differential yield dN_γ/dE_γ is a sum over specific final states

$$dN_\gamma/dE_\gamma = \sum_f B_f dN_\gamma^f/dE_\gamma,$$

(2)

where B_f is the branching fraction into a given final state. Branching fractions for χ pair annihilation in the CMSSM

---

[6] There is also an upper limit on spin-dependent LSP-proton scattering from the PICO-60 experiment using a ^{19}F target [143], with somewhat less sensitivity than the LZ limit.
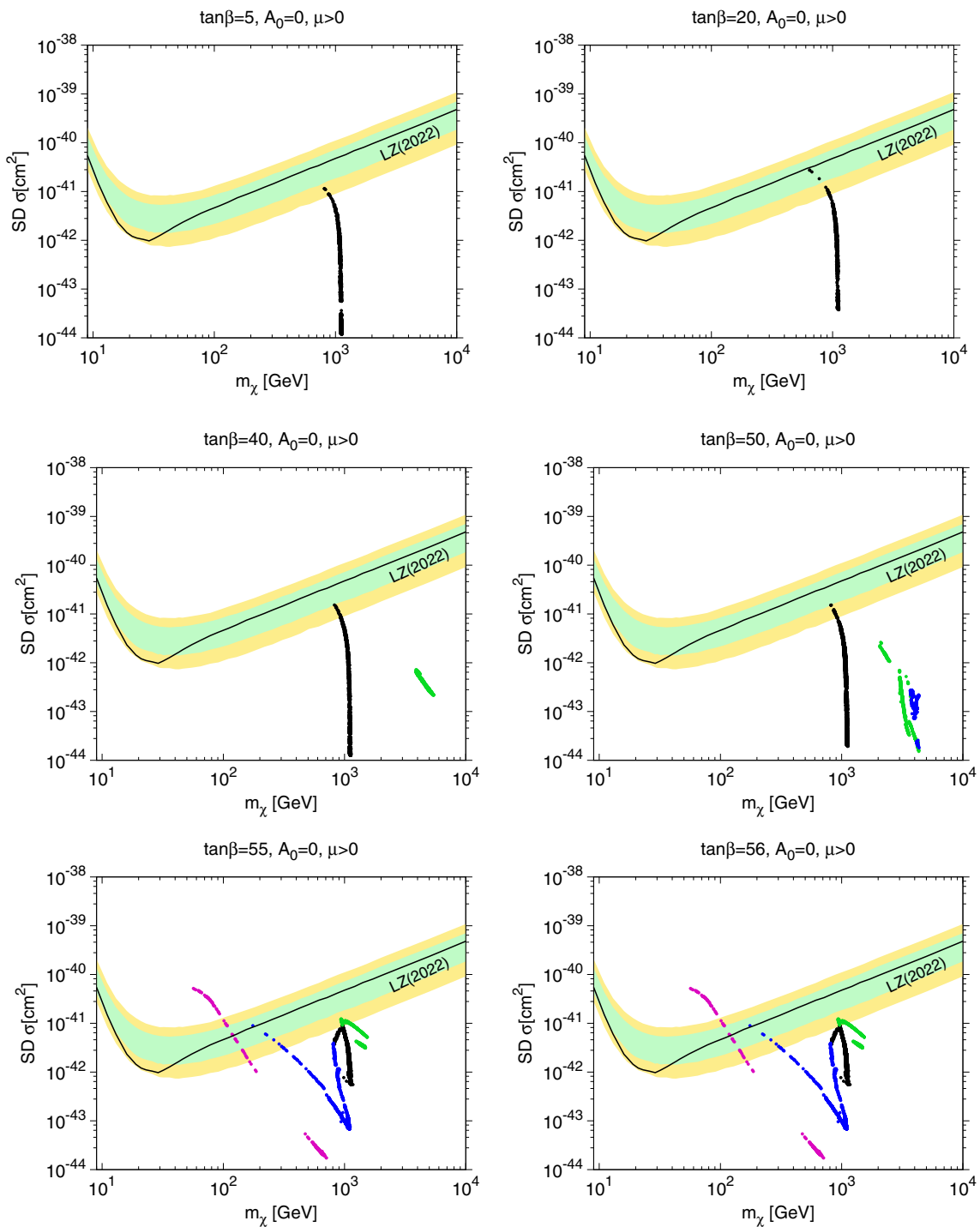
Fig. 9 Calculations of spin-independent WIMP-nucleon scattering for points along the dark matter strips for $\tan\beta = 5$, 20, 40, 50, 55 and 56 with $A_0 = 0$ and $\mu > 0$ compared with the LUX-ZEPLIN upper limit (solid black line). The green and yellow bands are the 1σ and 2σ LZ sensitivities

were studied in [51]. As described in detail there, we have used PYTHIA tool [153,154] in order to simulate the gamma fluxes produced in χ pair annihilations.

The second term in (1), the J factor, is the integral along the light of sight (l.o.s.) [155–157] through the DM density profile, ρ_{DM}, which is integrated over a solid angle, $\Delta\Omega$. The DM density profile may be given by the general expression

$$\rho_{DM}(r) = \frac{\rho_0}{(r/R)^c [1 + (r/R)^a]^{(b-c)/a}}, \qquad (3)$$

Fig. 10 Calculations of spin-dependent WIMP-nucleon scattering for points along the dark matter strips for $\tan\beta = 5, 20, 40, 50, 55$ and 56 with $A_0 = 0$ and $\mu > 0$ compared with the LUX-ZEPLIN upper limit on WIMP-neutron scattering (solid black line). The green and yellow bands are the 1σ and 2σ LZ sensitivities

where R is the characteristic length scale and a, b, c are parameters. In our analysis we assume that the DM distribution is a cuspy Navarro–Frenk–White (NFW) [158] profile with $a = c = 1.0$ and $\beta = 3.0$, i.e.

$$\rho_{DM}(r) = \frac{\rho r_s^3}{r(R+r)^2}. \tag{4}$$

We note that both the NFW and Burkert profiles [159] were studied in [45], whereas only the NFW profile was used in

a subsequent *Fermi*-LAT study [47], where it was found that the J factors for dSphs were relatively insensitive to the choice of DM distribution.

In our analysis, we have used the information on 25 Milky Way dSphs given in [47], including the `python` code provided by *Fermi* Tools for calculating the binned likelihood with energy dispersion. In order to use this code, we used the corresponding spacecraft data files for the dSphs and a background model, which are also provided by *Fermi* Tools. We used the energy range from 500 MeV to 500 GeV, divided into 30 logarithmic bins, and verified that our results are insensitive to various choices of the energy range and number of bins within the limits provided by *Fermi*-LAT. The times of the events we used range from 01/01/2009 to 01/01/2022. The window radius for searching these data is 15 degrees and the galactic coordinates for each dSph are taken from [47]. The selection of data sets is in accordance with the suggestion by the *Fermi*-LAT Collaboration.

After completing the analysis using *Fermi* Tools, we have evaluated the signals in the framework of the CMSSM, following the approach used previously in a study of the prospective γ signal from the GC [51]. We calculate the χ^2 likelihood function as follows:

$$\chi^2 = \sum_{i=1}^{n_{bins}} \frac{(d_i - (b_i + s_i))^2}{\sigma_i^2}, \tag{5}$$

where $n_{bins} = 30$ is the number of logarithmic bins in the energy range analyzed, d_i is the number of data counts per bin, b_i is the expected background provided by *Fermi* Tools [47], and s_i is the signal due to DM annihilations in each bin. The quantity σ_i is defined from

$$\sigma_i^2 = d_i + \sigma_{ea}^2, \tag{6}$$

where σ_{ea} is the systematic uncertainty in the effective area [51]. We evaluate the χ^2 contribution for each dSph separately.

Figure 11 displays our evaluations of the contribution to the global likelihood function, $\Delta\chi^2$, from the aggregated *Fermi*-LAT data on γ-rays from dSphs for the same values of $\tan\beta$ as in previous figures. We see that $\Delta\chi^2 \lesssim 0.1$ for $\tan\beta \leq 40$, and hence is negligible in these cases. However, the situation is quite different for $\tan\beta \geq 50$, as seen in the middle right and bottom panels of Fig. 11. Values of $\Delta\chi^2 \sim 10$ are reached in the well-tempered/funnel regions (blue) where $m_\chi \simeq 4$ TeV for $\tan\beta = 50$, $\simeq 1.1$ TeV for $\tan\beta = 55$ and $m_\chi \simeq 0.9$ TeV for $\tan\beta = 56$, excluding points in these regions, where the LSP annihilates mainly into $\bar{b}b$ final states through direct-channel H/A resonances. However, these points are already excluded by the calculation of m_h, as seen in Fig. 8. We note also that when $\tan\beta = 55$ and 56, $\Delta\chi^2$ reaches ~ 2 for funnel points with $m_\chi \simeq$

650 GeV. This is significant though not sufficient to exclude these points, which are in any case excluded by the constraint on m_h.

4.3.2 Limit on γ flux from the Galactic Centre

The production of γ rays near the GC was studied as a possible signature of the CMSSM in [51], whose analysis we follow here. Modelling the DM density near the GC entails significant uncertainties. The NFW model is frequently taken as a default, but other possibilities have been considered for comparison. For example, the H.E.S.S. Collaboration considered recently [52,53] an Einasto profile that would strengthen the prospective flux limit on annihilations of an LSP weighing 1 TeV by a factor > 2, and [160] considered a FIRE simulation that would strengthen the limit by a factor > 4. In a spirit of conservatism, here we use an NFW profile for setting constraints from data on the γ flux from near the GC.

Assuming the NFW profile, the recent H.E.S.S. analysis [52,53] finds a 95% CL upper limit on the cross section for LSP-LSP annihilation to W^+W^- that is stronger than that derived from the *Fermi*-LAT data on dSphs for $m_{LSP} \gtrsim 0.4$ TeV, which is the mass range of most interest for our analysis. However, in the CMSSM the branching fraction for W^+W^- final states is $< 100\%$, so other annihilation modes must be taken into account, which we do when comparing the sensitivities of the *Fermi*-LAT dSph and H.E.S.S. GC data in our analysis.

Figure 12 displays the contributions, $\Delta\chi^2$, to the global likelihood function provided by H.E.S.S. searches for γ-rays from near the GC in the framework of the CMSSM for $A_0 = 0$, $\mu > 0$ and our standard choices of $\tan\beta$. The general features are quite similar the those of the corresponding plots for the *Fermi*-LAT dSph analysis shown in Fig. 11. The values of $\Delta\chi^2$ provided by the H.E.S.S. data are larger than for the *Fermi*-LAT dSph data for $\tan\beta \leq 40$, though still small. There are non-negligible peaks in $\Delta\chi^2$ for $\tan\beta \geq 50$, which are again larger than those provided by the *Fermi*-LAT dSph data, but the two sets of data yield similar constraints away from the peaks. Once again, the points excluded by the H.E.S.S. GC γ-ray constraint also correspond to values of m_h that are too small, as seen in Fig. 8.[7]

4.3.3 Limit on energetic neutrinos from the Sun

The principle of the search for energetic neutrinos from the Sun [56–63] is that an LSP may scatter during passage through the Sun, losing energy and becoming gravitational bound in an elliptical orbit with perihelion smaller than the solar radius. The LSP will in general scatter again during

---

[7] The projected increase in sensitivity offered by CTA [161] would probe a larger range of funnel points.
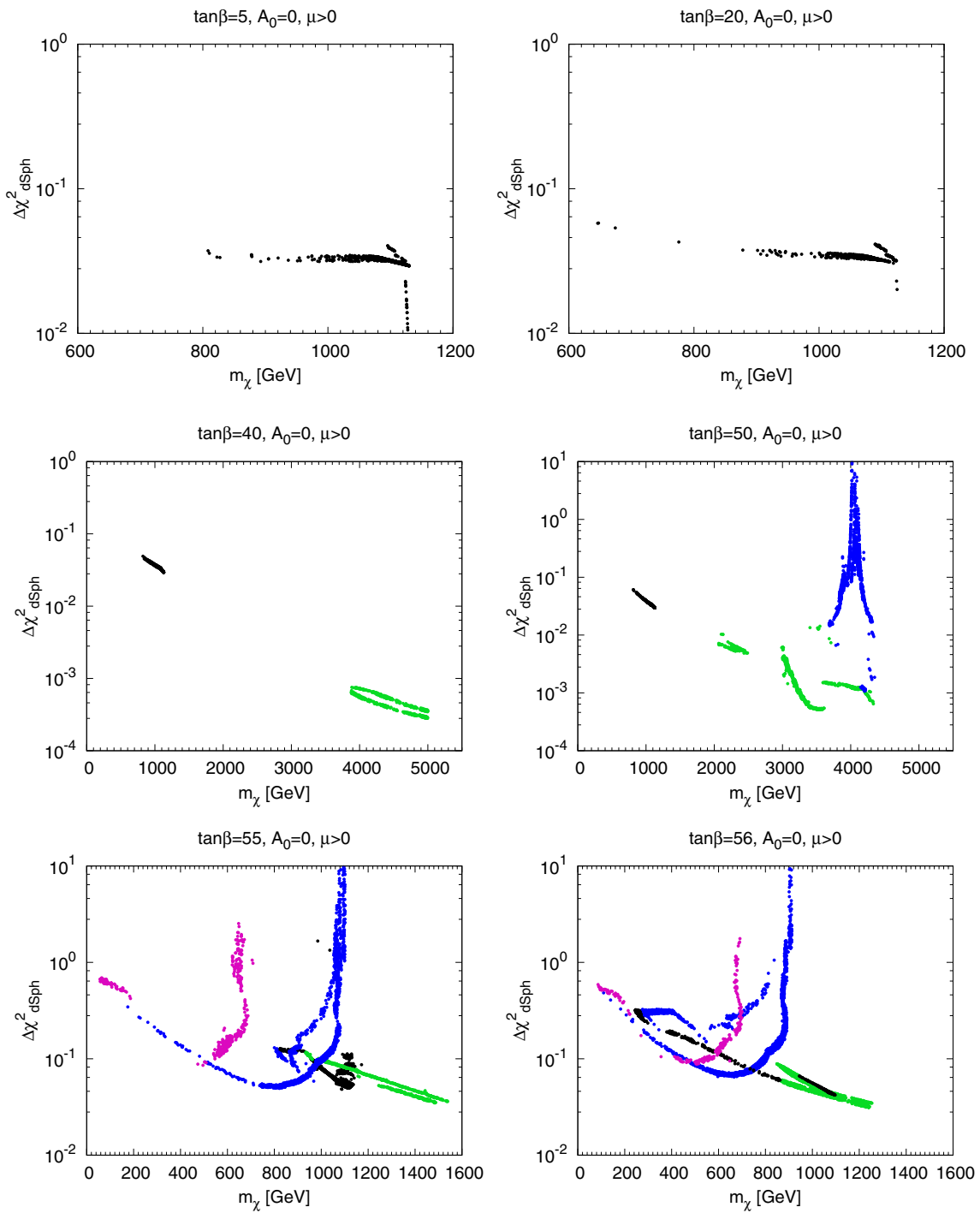
Fig. 11 Contributions to the global χ^2 likelihood function from a comparison of the *Fermi*-LAT upper limit on the flux of γ-rays from dwarf spheroidal satellite galaxies with calculations for points along the dark matter strips for $\tan\beta = 5, 20, 40, 50, 55$ and 56 with $A_0 = 0$ and $\mu > 0$

subsequent passages through the Sun, losing more energy each time and eventually settling into a thermal distribution inside the Sun. This distribution eventually equilibrates with a density that balances the LSP capture rate, C, with the loss of LSPs via annihilation, $2\Gamma_A$ where Γ_A is the annihilation rate. The annihilation rate in equilibrium is then determined

by the capture rate:

$$\Gamma_A = \frac{1}{2}C. \tag{7}$$

We note that this relation is not universal, as equilibrium may not be reached if C is too small. However, this is not an issue
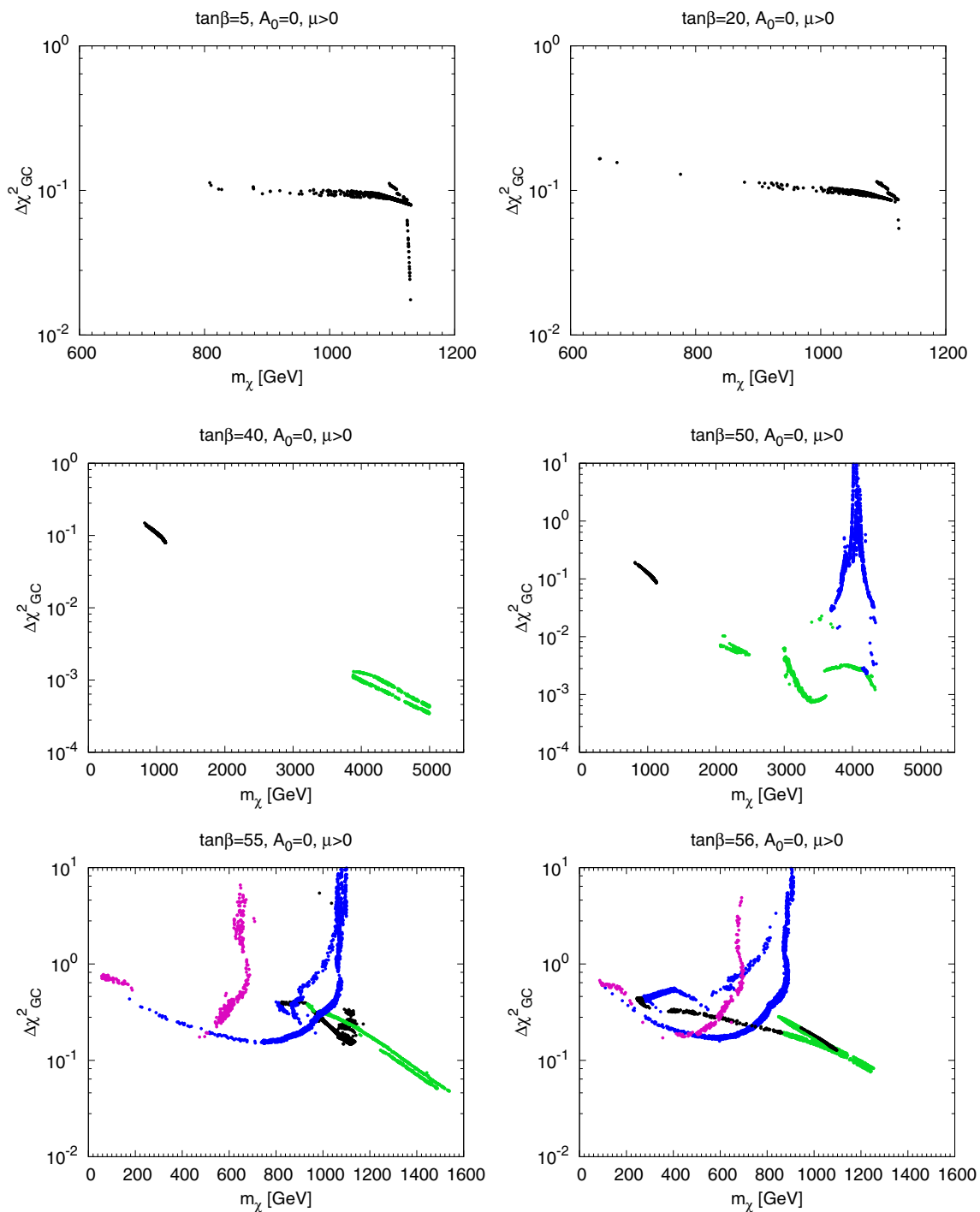
Fig. 12 Contributions to the global χ^2 likelihood function from a comparison of the H.E.S.S. upper limit on the flux of γ-rays from the Galactic Centre with calculations for points along the dark matter strips for $\tan\beta = 5, 20, 40, 50, 55$ and 56 with $A_0 = 0$ and $\mu > 0$

for the CMSSM scenarios we consider here, for which Eq. (7) is a good approximation [162,163].

Since nuclear matter in the Sun is largely composed of individual protons, the capture rate receives an important contribution from spin-dependent LSP-proton scattering, and limits on energetic solar neutrinos are occasionally inter-preted as upper limits on spin-dependent LSP-proton scat-tering. However, the Sun also contains a significant fraction by mass of ^{4}He, as well as trace amounts of heavier nuclei, so that spin-independent LSP-nucleon scattering is also poten-tially important. Both spin-independent and spin-dependent scattering are included in our calculation of the capture rate.

The calculation of the fluxes of the different neutrino species is straightforward, and we follow the analysis in [162,163]. The experimental observable is the flux of muons, which may be produced by either muon or tau neutrinos reaching Earth. We use the IceCube [64–66] upper limit on the flux of energetic muons from the Sun to constrain CMSSM parameters, taking into account the branching fractions for annihilations into different final states, e.g., $W^+W^-, \tau^+\tau^-, \ldots$ that are predicted at each point in the parameter space.

For the calculation of the corresponding $\Delta\chi^2$ we are employing the `nulike` software [164], following the likelihood estimation described in [64,164]. In addition, for the calculation of the likelihood we are taking into account the 79-string IceCube data, that is known to provide improved limits on WIMP dark matter searches [165]. As the basis for the $\Delta\chi^2$ we are plotting, we are using the p-value output from the `nulike` code.

The results of our analysis of the IceCube muon flux limits for $\tan\beta = 5, 20, 40, 50, 55$ and 56 are shown in Fig. 13. We see that for $m_\chi \lesssim 900$ GeV and $\tan\beta \leq 50$ the IceCube constraints contribute $2 \gtrsim \Delta\chi^2 \gtrsim 1$, not negligible, but insufficient to exclude any range of parameters. The $\tan\beta \leq 50$ points with larger LSP masses make negligible contributions to the χ^2 function. For $\tan\beta = 55$ there are points with 900 GeV $\lesssim m_\chi \lesssim 1400$ GeV that have $\Delta\chi^2 \gtrsim 1$, but there is again no exclusion. The only points excluded by the Ice-Cube muon flux limits are focus points for $\tan\beta = 56$ with 250 GeV $\lesssim m_\chi \lesssim 850$ GeV and some well-tempered points with larger m_χ. However, these points were already excluded because they correspond to values of m_h that are too low, as seen in Fig. 8, and by spin-independent cross sections that are too high as seen in Fig. 9.
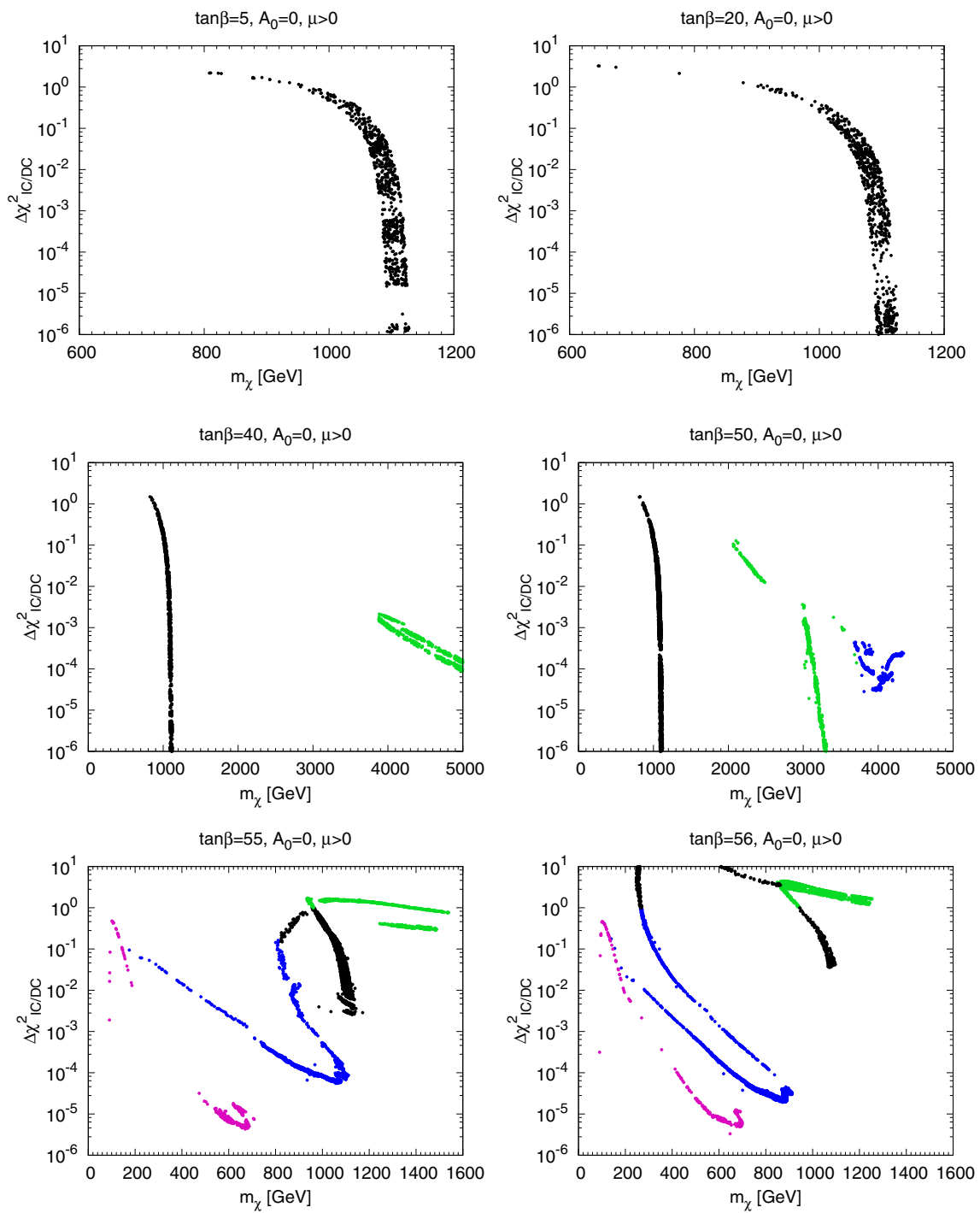
5 Combined results

Figures 14 and 15 display for $A_0 = 0$, $\mu > 0$ and our standard set of $\tan\beta$ values the results that we obtain by combining all the individual constraints discussed above, allowing uncertainties in the calculation of the Higgs mass $\Delta m_h = 1.5$ GeV and 0.5 GeV, respectively. In the case of $\tan\beta = 5$ and $\Delta m_h = 1.5$ GeV (top left panel of Fig. 14) the m_h and spin-independent scattering constraints combine to exclude values of $m_{1/2} \lesssim 7$ TeV, increasing to ~ 9 TeV for $\Delta m_h \sim 0.5$ GeV (top left panel of Fig. 15).[8] For $\tan\beta = 5$, the Higgs mass constraint is dominant. There are analogous exclusions for $\tan\beta = 20$ and 40, but extending only to lower values of $m_{1/2} \lesssim 4$ TeV, where the lower limit is determined by the spin-independent scattering constraint. In

the case of $\tan\beta = 50$, these constraints combine to exclude the funnel region and also the part of the focus-point strip with $m_{1/2} \lesssim 3.5$ TeV. There is also a small region of the focus-point strip with $m_{1/2} \gtrsim 6.5$ TeV that is excluded by the LHC measurement of m_h. We also see that most of the well-tempered strip allowed by m_h is excluded by σ^{SI}, leaving only a small set of points near $m_{1/2} \simeq 7$ TeV. Finally, we find that all of the strips for $\tan\beta = 55$ and 56 are excluded: the former by a combination of m_h and spin-independent scattering, and the latter by m_h alone. The other constraints considered also exclude independently parts of the regions excluded by m_h and spin-independent scattering, but no supplementary regions.

6 The case $A_0 = 3\,m_0$, $\mu > 0$

For $A_0 = 0$ and any fixed value of $m_{1/2}$, radiative electroweak symmetry breaking, i.e. a solution for the Higgs vevs by minimizing the Higgs potential, is no longer possible for sufficiently large m_0. This boundary is adjacent to the focus-point region where μ is driven to zero. This boundary moves to higher values of m_0 as A_0/m_0 increases. In addition, when A_0/m_0 is increased, there is increased splitting in the squark sector, and most notably, one of the stop masses becomes relatively light and comparable to the LSP mass allowing for the possibility that LSP-stop coannihilations determine the relic density [15,112–119,124]. When this occurs, there is again a thin dark matter strip adjacent to the boundary of the region where the light stop becomes the LSP. At still higher m_0, the lighter stop becomes tachyonic. Examples of the stop coannihilation strips for the representative choice $A_0/m_0 = 3$ with $\tan\beta = 5$ and $\tan\beta = 20$ are shown in the top left panels of Figs. 16 and 17. Along these strips, the complicated interplay of dark matter mechanisms such as annihilation via s-channel resonances, well-tempered neutralino composition, etc., does not recur, and there are no other dark matter strips of interest. The uncertainty in the `FeynHiggs 2.18.1` calculation of m_h is much larger for $A_0 = 3\,m_0$ than for $A_0 = 0$, with $\Delta m_h \gtrsim 3$ GeV. This should be borne in mind when interpreting the top right panels of Figs. 16 and 17. In particular, it implies that none of the displayed portions of the stop-coannihilation strips can be excluded on the basis of m_h. When $\tan\beta = 5$, the 1-σ range of m_h along the dark matter strip extends down to $m_{1/2} \sim 3$ TeV, well above the current reach of the LHC. On the other hand, the 1-σ range of m_h along the dark matter strip for $\tan\beta = 20$ extends down to $m_{1/2} \sim 1.4$ TeV, where $m_\chi \simeq 630$ GeV and $m_{\tilde{t}_1} \simeq 700$ GeV, coinciding with the current reach of LHC stop searches for the case of a compressed spectrum [166], and we find similar results for larger $\tan\beta$. However, the constraints from direct and indirect searches for astrophysical dark matter are not

---

[8] Note that the calculated uncertainty for $\tan\beta = 5$ is approximately 0.7 GeV, but ~ 0.5 GeV for all higher values of $\tan\beta$.

Fig. 13 Contributions to the global χ^2 likelihood function from a comparison of the IceCube upper limit on the muon flux generated by energetic neutrinos produced by WIMP annihilations in the core of the Sun [64–66] with calculations for points along the dark matter strips for $\tan\beta = 5$, 20, 40, 50, 55 and 56 with $A_0 = 0$ and $\mu > 0$
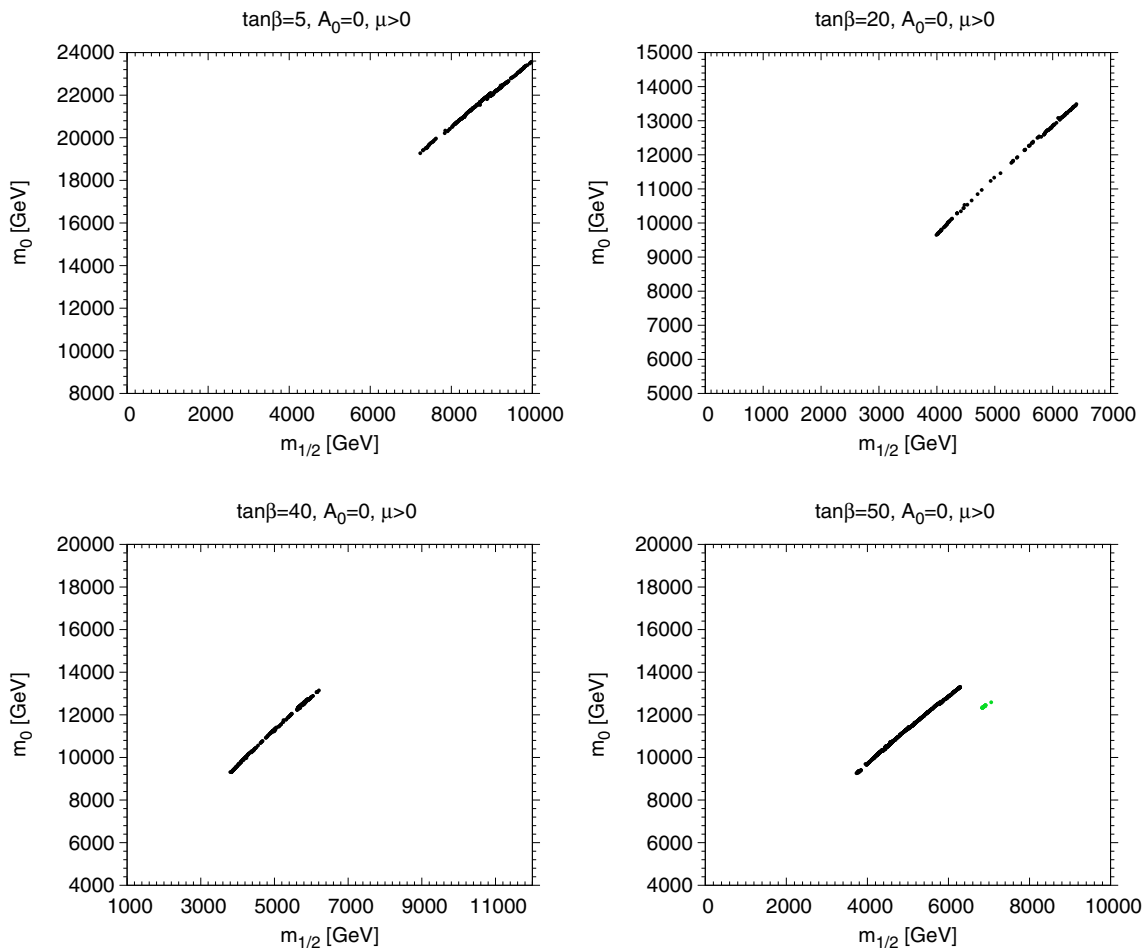
Fig. 14 The portions of the dark matter strips for $\tan\beta = 5$, 20, 40 and 50, calculated assuming $A_0 = 0$ and $\mu > 0$, that are allowed by all the constraints, assuming an uncertainty of 1.5 GeV in the calculation of m_h. There are no allowed regions for $\tan\beta = 55$ or 56

relevant along the stop coannihilation strip, as seen in the bottom 4 panels of Figs. 16 and 17.

We note that the $\Delta\chi^2$ related to neutrino searches at Ice-Cube is significantly suppressed in this case. This is due to the fact that in the stop coannihilation region both the scalar and the spin-dependent direct cross-sections are almost five orders of magnitude smaller than in the cosmologically acceptable higgsino region for the case $A_0 = 0$. This results in an annihilation rate in the Sun which is about eleven orders of magnitude smaller and the same applies to the muon fluxes. Thus, the resulting $\Delta\chi^2$ is suppressed by almost nineteen orders of magnitude.

7 The case $\mu < 0$

The case $A_0 = 0$ and $\mu < 0$ is also simpler than $A_0 = 0$ and $\mu > 0$. As seen in the illustrative examples in Fig. 18 for $\tan\beta = 5$ and Fig. 19 for $\tan\beta = 40$, there is only a single dark matter strip close to the boundary of electroweak

symmetry breaking. Overall, the results are very similar to those for $\mu > 0$ and the same values of $\tan\beta$, apart from the absence of the green well-tempered/funnel strip that appears below the focus-point strip in the $(m_{1/2}, m_0)$ plane when $\mu > 0$ and $\tan\beta = 40$. As for $\mu > 0$, m_h again provides the strongest constraint for $A_0 = 0$ and $\mu < 0$, as seen in the top right panels of Figs. 18 and 19. The direct search for spin-independent dark matter scattering also imposes an interesting constraint, as seen in the middle left panels of Figs. 18 and 19, excluding a range of LSP masses $\lesssim 1$ TeV that are, however, also excluded by m_h. The searches for γ-rays from dSphs and the Galactic Centre are not constraining, as seen in the middle right and bottom left panels of these figures. Finally, we note that a range of neutralino masses ~ 1 TeV that are excluded by m_h comes under some pressure from the IceCube search for energetic solar neutrinos, as seen in the bottom right panels of Figs. 18 and 19. The portions of the dark matter strips for $\tan\beta = 5$ and 40 that are allowed by all the constraints, assuming an uncertainty of 1.5 (0.5) GeV
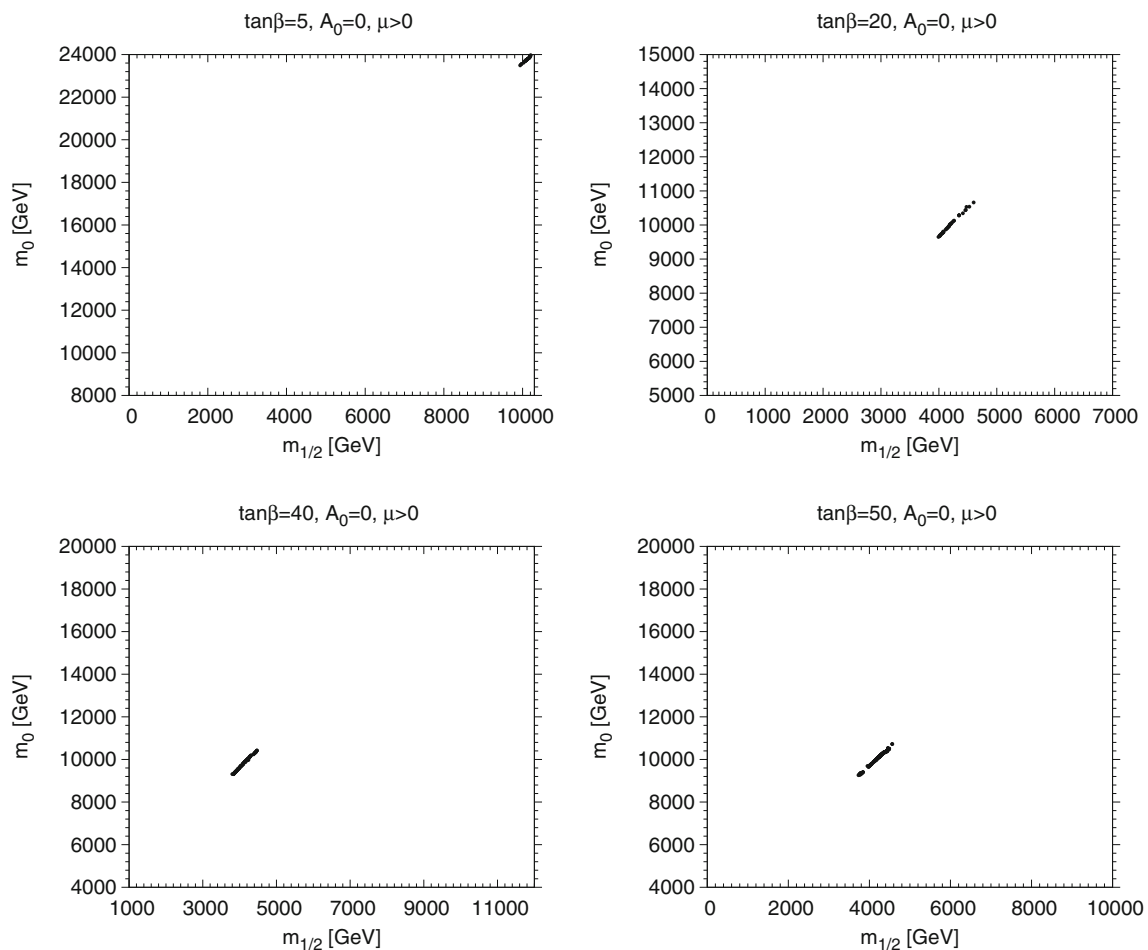
Fig. 15 As in Fig. 14, but assuming an uncertainty of 0.5 GeV in the calculation of m_h

in the calculation of m_h, are shown in the upper (lower) pair of panels of Fig. 20.

8 Conclusions

We have analyzed in this paper the viability of the CMSSM in light of the available phenomenological constraints, assuming that R-parity is conserved and the lightest supersymmetric particle is a neutralino that provides the cosmological dark matter. The CMSSM framework assumes universality of all scalar masses, gaugino masses and A-terms separately at the GUT scale. We also assume a standard thermal freeze-out scenario for the relic density. Relaxing these assumptions would correspondingly relax the constraints derived here, and enlarge the regions of parameters where supersymmetry can survive. However, these assumptions restrict the allowed CMSSM parameter space to narrow strips where the relic dark matter density is compatible with the narrow range permitted by *Planck* and other measurements. As we have discussed in detail in Sect. 2,

there are several such strips when the ratio of Higgs vevs $\tan \beta \geq 40$, the trilinear supersymmetry-breaking parameter $A_0 = 0$, and the Higgsino mixing parameter $\mu > 0$. On the other hand, when $\tan \beta < 40$ or $\mu < 0$ there is a single CMSSM dark matter strip running close to the boundary of the region where electroweak symmetry breaking occurs. Similarly when $A_0 = 3\,m_0$, there is a single CMSSM dark matter strip running close to the boundary where the LSP and lighter stop are degenerate. As we have discussed in detail, when $A_0 = 0$ and $\mu > 0$ several different mechanisms may come into play simultaneously to bring the dark matter density into the allowed cosmological range, including focus-point and well-tempered neutralino effects, s-channel annihilations via heavy Higgs bosons. In contrast, the dominant dark matter mechanism when $A_0 = 3\,m_0$ is LSP coannihilation with stop squarks.

In Sect. 3 we have discussed the LHC constraints on parameter points along the CMSSM dark matter strips. We have found that direct LHC searches for sparticles do not constrain the CMSSM as strongly as the indirect constraint provided by the LHC measurement of the Higgs mass and cal-
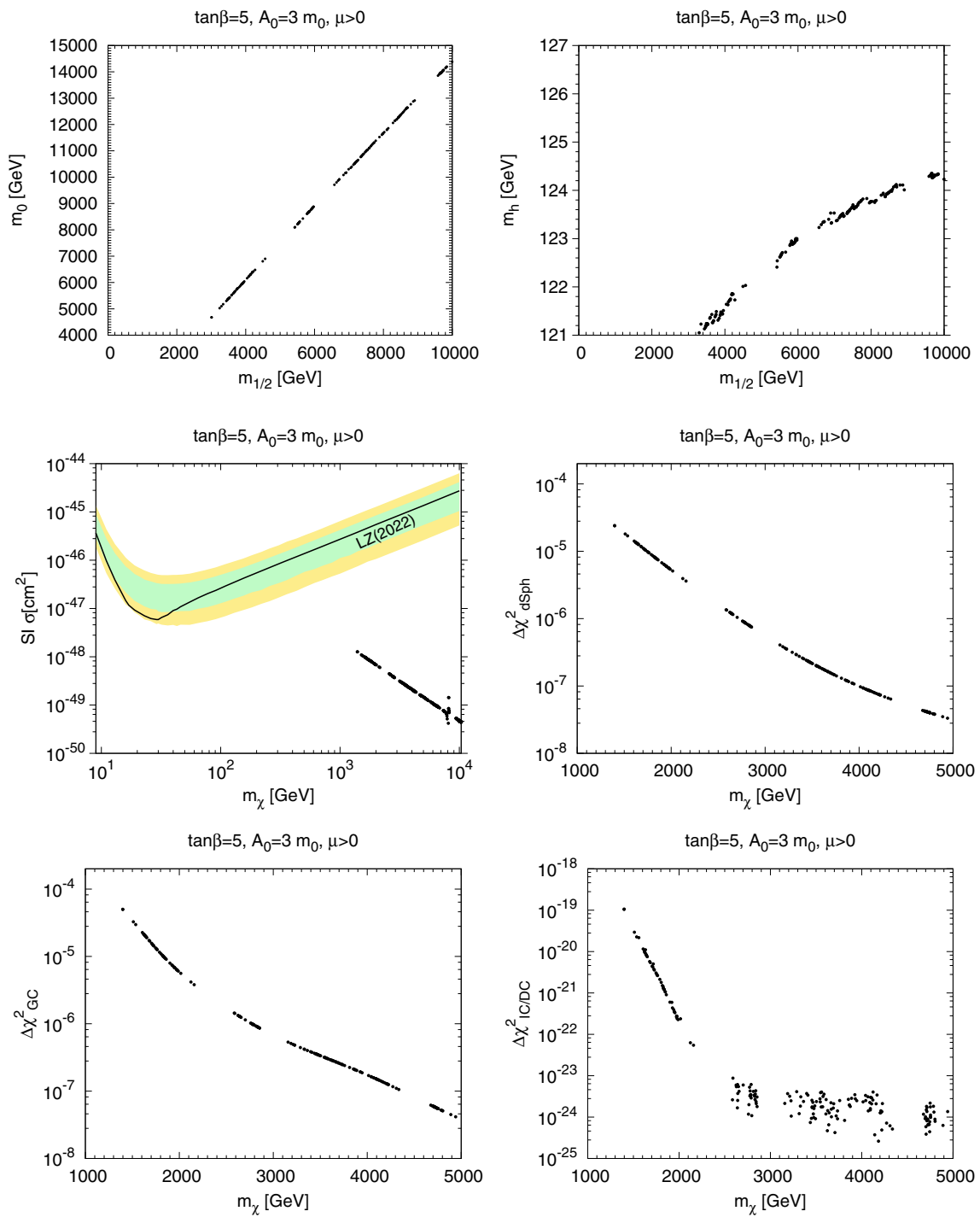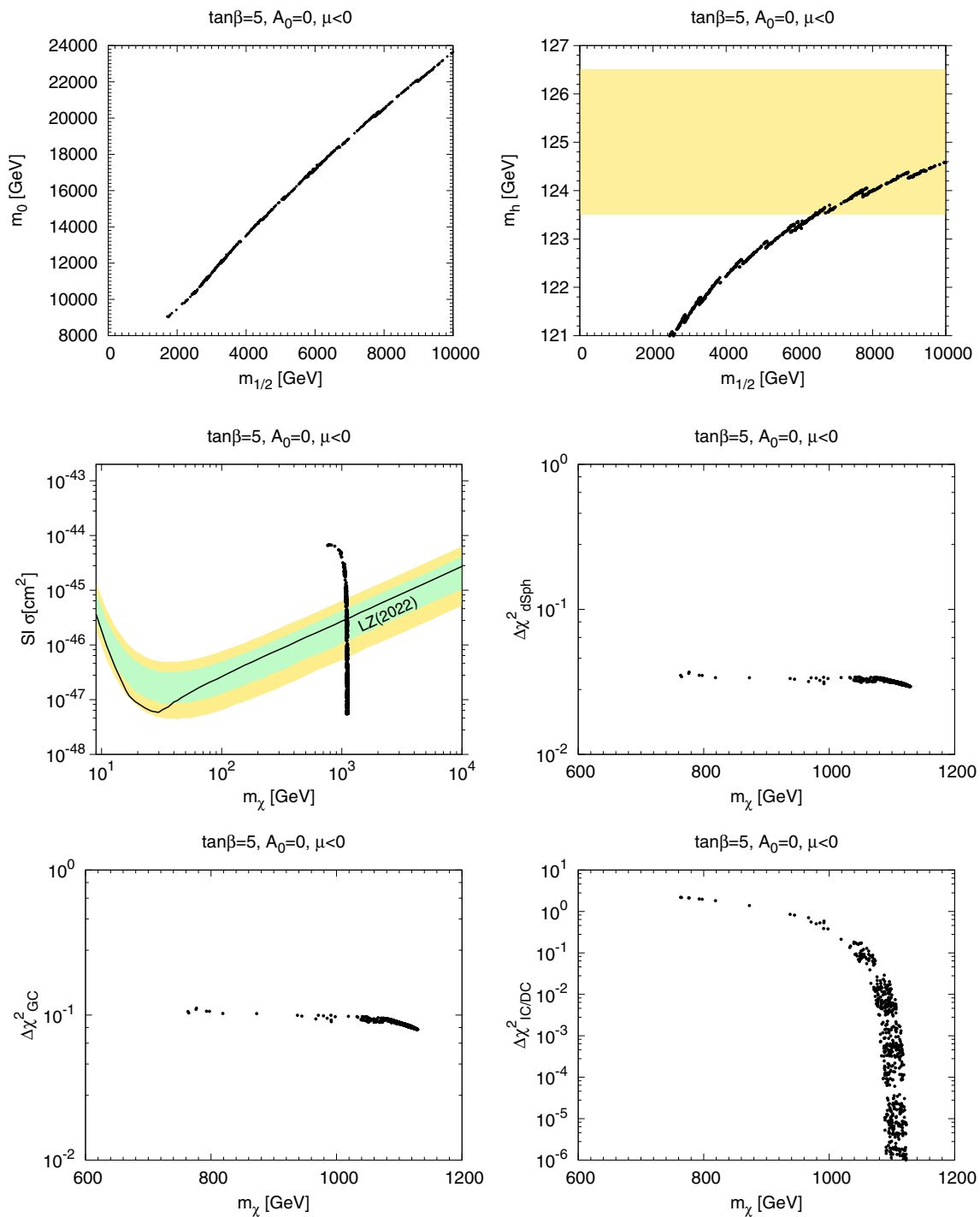
Fig. 16 The dark matter strip, m_h constraint, spin-independent direct scattering constraint, $\Delta\chi^2$ from *Fermi*-LAT dSph and H.E.S.S. GC γ-ray and Icecube solar ν signals for the case $\tan\beta = 5$, $A_0 = 3m_0$ and $\mu > 0$
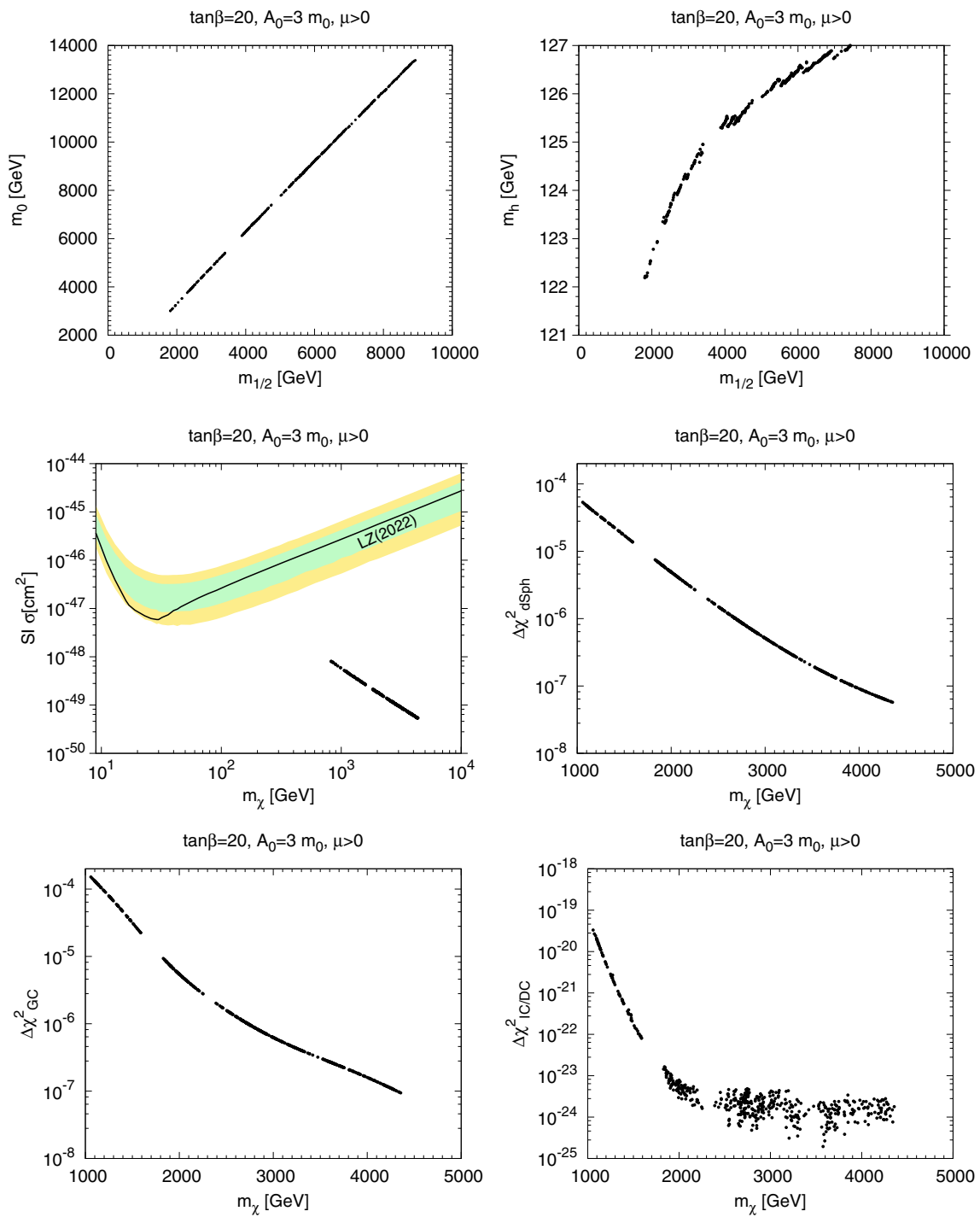
Fig. 17 The dark matter strip, m_h constraint, spin-independent direct scattering constraint, $\Delta\chi^2$ from *Fermi*-LAT dSph and H.E.S.S. GC γ-ray and Icecube solar ν signals for the case $\tan\beta = 20$, $A_0 = 3m_0$ and $\mu > 0$

Fig. 18 The $(m_{1/2}, m_0)$ plane, the m_h, spin-independent direct scattering and indirect constraints for the case $\tan\beta = 5$, $A_0 = 0$ and $\mu < 0$

culations of m_h using `FeynHiggs 2.18.1`. These favour relatively large values of the soft supersymmetry-breaking parameters.

In Sect. 4 we have discussed the constraints on the CMSSM provided by searches for astrophysical dark matter. These include the direct searches for dark matter scattering on nuclei via spin-independent and -dependent interactions. As

we have shown, the non-detection of spin-independent dark matter scattering imposes a stronger constraint. It excludes significant parts of the dark matter strips, while allowed parts are in general incompatible with the m_h constraint. We have also considered the constraints provided by searches for γ-rays from dwarf spheroidal galaxies and the Galactic Centre. These both exclude portions of the funnel strips for large
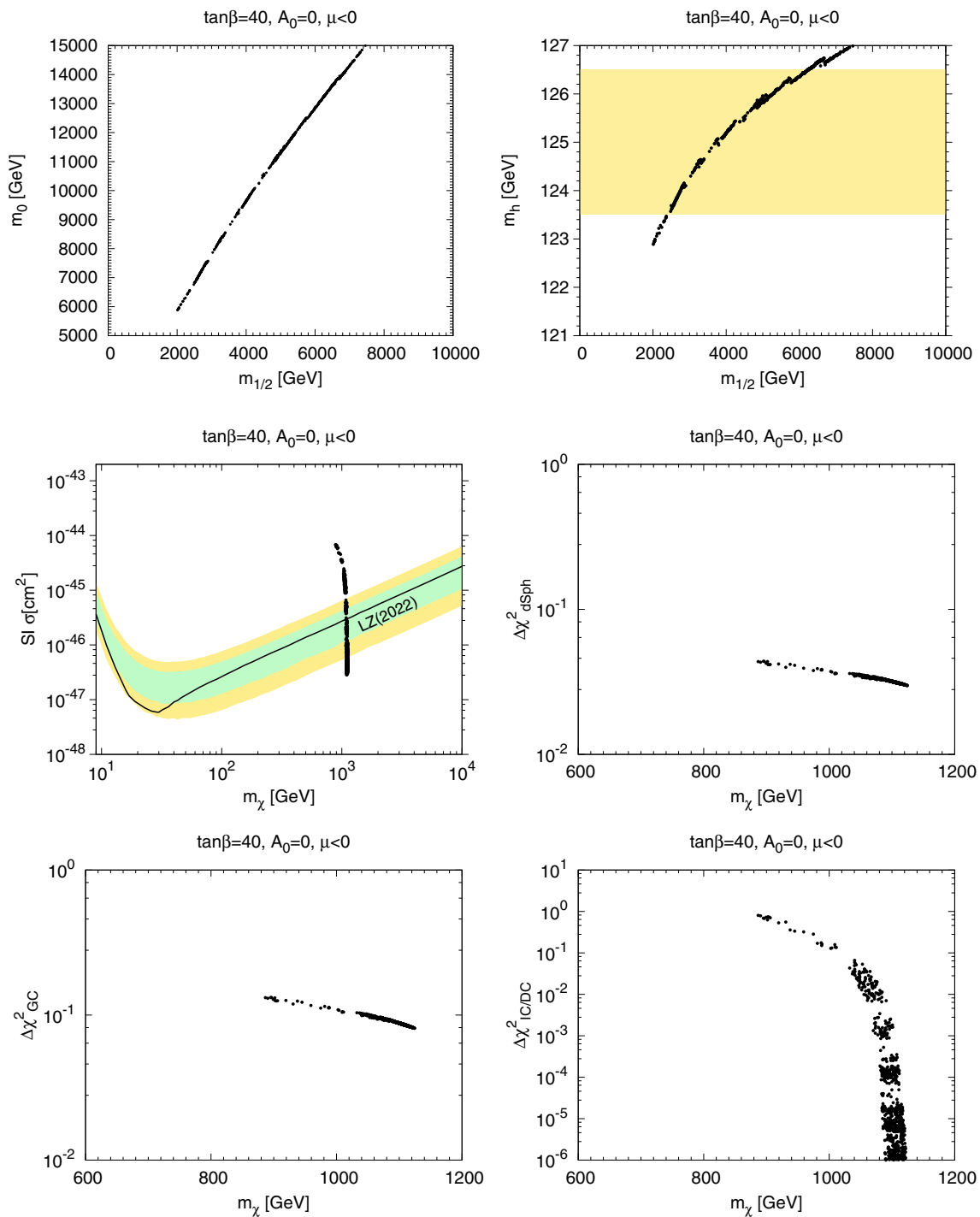
Fig. 19 As in Fig. 18, for the case $\tan\beta = 40$, $A_0 = 0$ and $\mu < 0$

$\tan\beta$, $A_0 = 0$ and $\mu > 0$, though these are also excluded by m_h constraint. The IceCube search for muons produced by energetic neutrinos generated by the annihilations of dark matter particles trapped inside the Sun excludes a range of CMSSM parameters at large $\tan\beta$, $A_0 = 0$ and $\mu > 0$ that are, however, also excluded by the m_h constraint.

The overall result of our analysis is that, whilst the searches for astrophysical dark matter do exclude portions of the CMSSM dark matter strips, these are mostly also covered by the m_h constraint, which is the most powerful when $A_0 = 0$. In this case, as seen in Figs. 14, 15 and 20, only very restricted portions of the CMSSM dark matter strips are allowed by m_h. The lengths of these allowed
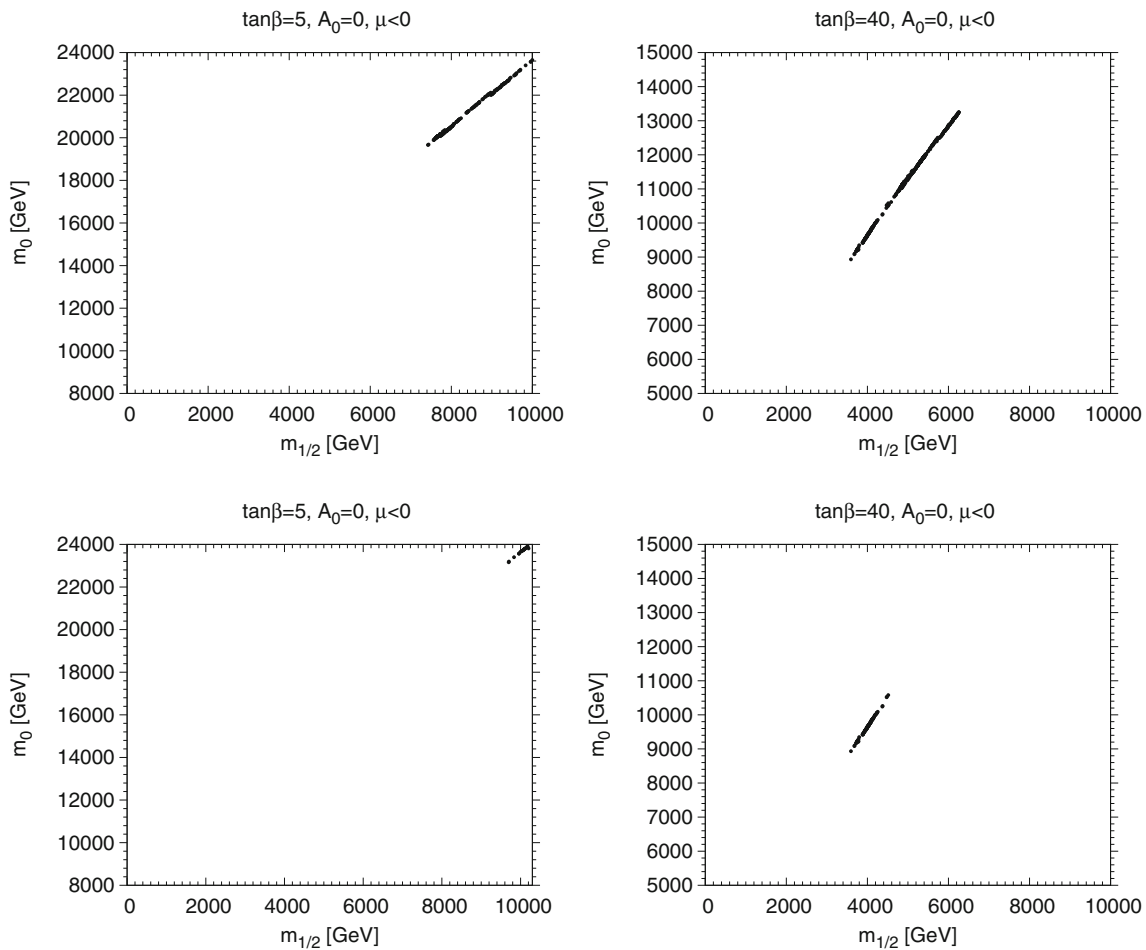
Fig. 20 The portions of the dark matter strips for $\tan \beta = 5$ and 40, calculated assuming $A_0 = 0$ and $\mu < 0$, that are allowed by all the constraints, assuming an uncertainty of 1.5 (0.5) GeV in the calculation of m_h in the upper (lower) pair of panels

portions are sensitive primarily to the assumed uncertainty in the calculation of m_h, which is typically ~ 0.5 GeV when $A_0 = 0$. This is significantly larger than the measurement uncertainty, which is between 0.1 and 0.2 GeV. We emphasize that the uncertainty in the m_h calculation is much greater when $A_0 = 3\, m_0, \gtrsim 3$ GeV, rendering it an ineffective constraint for $A_0 = 3\, m_0$, and note that the direct and indirect searches for astrophysical dark matter are also ineffective for this value of A_0.

For the moment the CMSSM survives *Planck*, the LHC, LUX-ZEPLIN, *Fermi*-LAT, H.E.S.S. and IceCube. However, our constraints push the supersymmetry breaking mass scale to $\mathcal{O}(10)$ TeV, larger than the scale originally associated with supersymmetry when proposed as a solution to the hierarchy problem. Nevertheless, supersymmetry at this scale still alleviates the hierarchy problem to some extent. In the future, the most immediate prospect for putting pressure on the CMSSM may be provided by future direct searches for spin-independent dark matter scattering, which could probe essentially all the strips for $A_0 = 0$ and either sign of μ

if their sensitivity reaches down to the neutrino 'floor' [71–73]. In the longer run, searches at FCC-hh or SppC offer good prospects for discovering supersymmetry within the CMSSM framework also when $A_0 \neq 0$ [167]. On the other hand, the astrophysical searches for dark matter are relatively unpromising for $A_0 = 3m_0$, and also have lacunae when $\mu < 0$. The CMSSM may survive a while yet.

Data Availability Statement This manuscript has no associated data or the data will not be deposited. [Authors' comment: This work is a phenomenological analysis.]

References

1. M. Drees, M.M. Nojiri, Phys. Rev. D **47**, 376 (1993). arXiv:hep-ph/9207234
2. G.L. Kane, C.F. Kolda, L. Roszkowski, J.D. Wells, Phys. Rev. D **49**, 6173 (1994). arXiv:hep-ph/9312272
3. J.R. Ellis, K.A. Olive, Y. Santoso, V.C. Spanos, Phys. Lett. B **565**, 176 (2003). arXiv:hep-ph/0303043
4. H. Baer, C. Balazs, JCAP **0305**, 006 (2003). arXiv:hep-ph/0303114
5. A.B. Lahanas, D.V. Nanopoulos, Phys. Lett. B **568**, 55 (2003). arXiv:hep-ph/0303130
6. U. Chattopadhyay, A. Corsetti, P. Nath, Phys. Rev. D **68**, 035005 (2003). arXiv:hep-ph/0303201
7. J. Ellis, K.A. Olive, Published in *Particle Dark Matter*, ed. by G. Bertone, pp. 142–163. arXiv:1001.3651 [astro-ph.CO]
8. J. Ellis, K.A. Olive, Eur. Phys. J. C **72**, 2005 (2012). arXiv:1202.3262 [hep-ph]
9. J. Cao, Z. Heng, D. Li, J.M. Yang, Phys. Lett. B **710**, 665–670 (2012). arXiv:1112.4391 [hep-ph]
10. O. Buchmueller et al., Eur. Phys. J. C **74**(3), 2809 (2014). arXiv:1312.5233 [hep-ph]
11. E. Bagnaschi, H. Bahl, J. Ellis, J. Evans, T. Hahn, S. Heinemeyer, W. Hollik, K. Olive, S. Passehr, H. Rzehak, I. Sobolev, G. Weiglein, J. Zheng, Eur. Phys. J. C **79**(2), 149 (2019). arXiv:1810.10905 [hep-ph]
12. J. Ellis, F. Luo, K.A. Olive, P. Sandick, Eur. Phys. J. C **73**(4), 2403 (2013). arXiv:1212.4476 [hep-ph]
13. O. Buchmueller, M. Citron, J. Ellis, S. Guha, J. Marrouche, K.A. Olive, K. de Vries, J. Zheng, Eur. Phys. J. C **75**(10), 469 (2015). arXiv:1505.04702 [hep-ph]. [Erratum: Eur. Phys. J. C **76**(4), 190 (2016)]
14. J. Ellis, J.L. Evans, F. Luo, N. Nagata, K.A. Olive, P. Sandick, Eur. Phys. J. C **76**(1), 8 (2016). arXiv:1509.08838 [hep-ph]
15. J. Ellis, J.L. Evans, F. Luo, K.A. Olive, J. Zheng, Eur. Phys. J. C **78**(5), 425 (2018). arXiv:1801.09855 [hep-ph]
16. J. Ellis, J.L. Evans, N. Nagata, K.A. Olive, L. Velasco-Sevilla, Eur. Phys. J. C **80**(4), 332 (2020). arXiv:1912.04888 [hep-ph]
17. M. Aaboud et al. (ATLAS Collaboration), JHEP **1806**, 107 (2018). arXiv:1711.01901 [hep-ex]
18. M. Aaboud et al. (ATLAS Collaboration), Phys. Rev. D **97**(11), 112001 (2018). arXiv:1712.02332 [hep-ex]
19. A.M. Sirunyan et al. (CMS Collaboration), Eur. Phys. J. C **77**(10), 710 (2017). arXiv:1705.04650 [hep-ex]
20. A.M. Sirunyan et al. (CMS Collaboration), JHEP **1805**, 025 (2018). arXiv:1802.02110 [hep-ex]
21. E. Aprile et al. (XENON Collaboration), Phys. Rev. Lett. **121**(11), 111302 (2018). arXiv:1805.12562 [astro-ph.CO]
22. D.S. Akerib et al. (LUX Collaboration), Phys. Rev. Lett. **118**(2), 021303 (2017). arXiv:1608.07648 [astro-ph.CO]
23. Q. Wang et al. (PandaX-II Collaboration), Chin. Phys. C **44**(12), 125001 (2020). arXiv:2007.15469 [astro-ph.CO]
24. Y. Meng et al. (PandaX-4T Collaboration), Phys. Rev. Lett. **127**(26), 261802 (2021). arXiv:2107.13438 [hep-ex]
25. J. Aalbers et al. (LUX-ZEPLIN Collaboration), arXiv:2207.03764 [hep-ex]
26. N. Aghanim et al. (Planck Collaboration), Astron. Astrophys. **641**, A6 (2020). arXiv:1807.06209 [astro-ph.CO]
27. G.B. Gelmini, P. Gondolo, Phys. Rev. D **74**, 023510 (2006). arXiv:hep-ph/0602230
28. G. Kane, K. Sinha, S. Watson, Int. J. Mod. Phys. D **24**(08), 1530022 (2015). arXiv:1502.07746 [hep-th]
29. G. Aad et al. (ATLAS Collaboration), Phys. Lett. B **716**, 1 (2012). arXiv:1207.7214 [hep-ex]
30. S. Chatrchyan et al. (CMS Collaboration), Phys. Lett. B **716**, 30 (2012). arXiv:1207.7235 [hep-ex]
31. G. Aad et al. (ATLAS and CMS Collaborations), Phys. Rev. Lett. **114**, 191803 (2015). arXiv:1503.07589 [hep-ex]
32. H. Bahl, T. Hahn, S. Heinemeyer, W. Hollik, S. Passehr, H. Rzehak, G. Weiglein, Comput. Phys. Commun. **249**, 107099 (2020). arXiv:1811.09073 [hep-ph]
33. J. Ellis, K. Olive, Y. Santoso, Phys. Lett. B **539**, 107 (2002). arXiv:hep-ph/0204192
34. J.R. Ellis, T. Falk, K.A. Olive, Y. Santoso, Nucl. Phys. B **652**, 259 (2003). arXiv:hep-ph/0210205
35. H. Baer, A. Mustafayev, S. Profumo, A. Belyaev, X. Tata, Phys. Rev. D **71**, 095008 (2005). arXiv:hep-ph/0412059
36. H. Baer, A. Mustafayev, S. Profumo, A. Belyaev, X. Tata, JHEP **0507**, 065 (2005). arXiv:hep-ph/0504001
37. J.R. Ellis, K.A. Olive, P. Sandick, Phys. Rev. D **78**, 075012 (2008). arXiv:0805.2343 [hep-ph]
38. N. Craig, arXiv:1309.0528 [hep-ph]
39. E.A. Bagnaschi, O. Buchmueller, R. Cavanaugh, M. Citron, A. De Roeck, M.J. Dolan, J.R. Ellis, H. Flächer, S. Heinemeyer, G. Isidori et al., Eur. Phys. J. C **75**, 500 (2015). arXiv:1508.01173 [hep-ph]
40. L. Maiani, in *Proceedings, Gif-sur-Yvette Summer School on Particle Physics* (1979), pp. 1–52
41. Gerard 't Hooft et al. (eds.), in *Recent Developments in Gauge Theories, Proceedings of the NATO Advanced Study Institute, Cargese, France, August 26–September 8, 1979. NATO Advanced Study Institutes Series: Series B, Physics*, vol. 59 (Plenum press, New York, 1980).Edward Witten, *Phys. Lett.* B105, 267, 1981
42. E. Witten, Phys. Lett. B **105**, 267 (1981)
43. L.E. Strigari, Phys. Rep. **531**, 1–88 (2013). arXiv:1211.7090 [astro-ph.CO]
44. T.R. Slatyer, SciPost Phys. Lect. Notes **53**, 1 (2022). arXiv:2109.02696 [hep-ph]
45. M. Ackermann et al. (Fermi-LAT Collaboration), Phys. Rev. D **89**, 042001 (2014). arXiv:1310.0828 [astro-ph.HE]
46. A. Drlica-Wagner et al. (Fermi-LAT and DES Collaborations), Astrophys. J. Lett. **809**(1), L4 (2015). arXiv:1503.02632 [astro-ph.HE]
47. M. Ackermann et al. (Fermi-LAT Collaboration), Phys. Rev. Lett. **115**(23), 231301 (2015). arXiv:1503.02641 [astro-ph.HE]
48. K. Boddy, J. Kumar, D. Marfatia, P. Sandick, Phys. Rev. D **97**(9), 095031 (2018). arXiv:1802.03826 [hep-ph]
49. S. Hoof, A. Geringer-Sameth, R. Trotta, JCAP **02**, 012 (2020). arXiv:1812.06986 [astro-ph.CO]
50. A. Alvarez, F. Calore, A. Genina, J. Read, P.D. Serpico, B. Zaldivar, JCAP **09**, 004 (2020). arXiv:2002.01229 [astro-ph.HE]
51. J. Ellis, K.A. Olive, V.C. Spanos, JCAP **10**, 024 (2011). arXiv:1106.0768 [hep-ph]

52. H. Abdalla et al. (H.E.S.S. Collaboration), Phys. Rev. Lett. **129**(11), 111101 (2022). arXiv:2207.10471 [astro-ph.HE]
53. H. Abdallah et al. (HESS), Phys. Rev. Lett. **120**(20), 201101 (2018). arXiv:1805.05741 [astro-ph.HE]
54. C. Johnson, R. Caputo, C. Karwin, S. Murgia, S. Ritz, J. Shelton, Phys. Rev. D **99**(10), 103007 (2019). arXiv:1904.06261 [astro-ph.HE]
55. K.N. Abazajian, S. Horiuchi, M. Kaplinghat, R.E. Keeley, O. Macias, Phys. Rev. D **102**(4), 043012 (2020). arXiv:2003.10416 [hep-ph]
56. J. Silk, K.A. Olive, M. Srednicki, Phys. Rev. Lett. **55**, 257 (1985)
57. M. Srednicki, K.A. Olive, J. Silk, Nucl. Phys. B **279**, 804 (1987)
58. J.S. Hagelin, K.W. Ng, K.A. Olive, Phys. Lett. B **180**, 375 (1986)
59. K.W. Ng, K.A. Olive, M. Srednicki, Phys. Lett. B **188**, 138 (1987)
60. T.K. Gaisser, G. Steigman, S. Tilav, Phys. Rev. D **34**, 2206 (1986)
61. F. Halzen, T. Stelzer, M. Kamionkowski, Phys. Rev. D **45**, 4439 (1992)
62. L. Bergstrom, J. Edsjo, P. Gondolo, Phys. Rev. D **55**, 1765 (1997). arXiv:hep-ph/9607237
63. N. Fornengo, A. Masiero, F.S. Queiroz, C.E. Yaguna, JCAP **12**, 012 (2017). arXiv:1710.02155 [hep-ph]
64. M.G. Aartsen et al. (IceCube Collaboration), JCAP **04**, 022 (2016). arXiv:1601.00653 [hep-ph]
65. M.G. Aartsen et al. (IceCube Collaboration), Eur. Phys. J. C **77**(3), 146 (2017). arXiv:1612.05949 [astro-ph.HE]. [Erratum: Eur. Phys. J. C **79**(3), 214 (2019)]
66. R. Abbasi et al. (IceCube Collaboration), Phys. Rev. D **105**(6), 062004 (2022). arXiv:2111.09970 [astro-ph.HE]
67. J.L. Feng, K.T. Matchev, T. Moroi, Phys. Rev. Lett. **84**, 2322 (2000). arXiv:hep-ph/9908309
68. H. Baer, T. Krupovnickas, S. Profumo, P. Ullio, JHEP **0510**, 020 (2005). arXiv:hep-ph/0507282
69. J.L. Feng, K.T. Matchev, D. Sanford, Phys. Rev. D **85**, 075007 (2012). arXiv:1112.3021 [hep-ph]
70. P. Draper, J. Feng, P. Kant, S. Profumo, D. Sanford, Phys. Rev. D **88**, 015025 (2013). arXiv:1304.1159 [hep-ph]
71. J. Billard, L. Strigari, E. Figueroa-Feliciano, Phys. Rev. D **89**(2), 023524 (2014). arXiv:1307.5458 [hep-ph]
72. P. Cushman, C. Galbiati, D.N. McKinsey, H. Robertson, T.M.P. Tait, D. Bauer, A. Borgland, B. Cabrera et al., Snowmass working group report: WIMP dark matter direct detection. arXiv:1310.8327 [hep-ex]
73. L.E. Strigari, Phys. Rev. D **93**(10), 103534 (2016). arXiv:1604.00729 [astro-ph.CO]
74. T. Aoyama et al., Phys. Rep. **887**, 1–166 (2020). arXiv:2006.04822 [hep-ph]
75. M. Davier, A. Hoecker, B. Malaescu, Z. Zhang, Eur. Phys. J. C **71**, 1515 (2011). arXiv:1010.4180 [hep-ph]. [Erratum: Eur. Phys. J. C **72**, 1874 (2012)]
76. A. Kurz, T. Liu, P. Marquard, M. Steinhauser, Phys. Lett. B **734**, 144–147 (2014). arXiv:1403.6400 [hep-ph]
77. G. Colangelo, M. Hoferichter, P. Stoffer, JHEP **02**, 006 (2019). arXiv:1810.00007 [hep-ph]
78. M. Hoferichter, B.L. Hoid, B. Kubis, JHEP **08**, 137 (2019). arXiv:1907.01556 [hep-ph]
79. M. Davier, A. Hoecker, B. Malaescu, Z. Zhang, Eur. Phys. J. C **80**(3), 241 (2020). arXiv:1908.00921 [hep-ph]. [Erratum: Eur. Phys. J. C **80**(5), 410 (2020)]
80. A. Keshavarzi, D. Nomura, T. Teubner, Phys. Rev. D **101**(1), 014029 (2020). arXiv:1911.00367 [hep-ph]
81. H.N. Brown et al. (Muon g-2 Collaboration), Phys. Rev. Lett. **86**, 2227–2231 (2001). arXiv:hep-ex/0102017
82. G.W. Bennett et al. (Muon g-2 Collaboration), Phys. Rev. D **73**, 072003 (2006). arXiv:hep-ex/0602035
83. B. Abi et al. (Muon g-2 Collaboration), Phys. Rev. Lett. **126**, 141801 (2021). arXiv:2104.03281 [hep-ex]

84. L.L. Everett, G.L. Kane, S. Rigolin, L. Wang, Phys. Rev. Lett. **86**, 3484 (2001). arXiv:hep-ph/0102145
85. J.L. Feng, K.T. Matchev, Phys. Rev. Lett. **86**, 3480 (2001). arXiv:hep-ph/0102146
86. E.A. Baltz, P. Gondolo, Phys. Rev. Lett. **86**, 5004 (2001). arXiv:hep-ph/0102147
87. U. Chattopadhyay, P. Nath, Phys. Rev. Lett. **86**, 5854 (2001). arXiv:hep-ph/0102157
88. S. Komine, T. Moroi, M. Yamaguchi, Phys. Lett. B **506**, 93 (2001). arXiv:hep-ph/0102204
89. J. Hisano, K. Tobe, Phys. Lett. B **510**, 197–204 (2001). arXiv:hep-ph/0102315
90. J.R. Ellis, D.V. Nanopoulos, K.A. Olive, Phys. Lett. B **508**, 65–73 (2001). arXiv:hep-ph/0102331
91. R. Arnowitt, B. Dutta, B. Hu, Y. Santoso, Phys. Lett. B **505**, 177 (2001). arXiv:hep-ph/0102344
92. S.P. Martin, J.D. Wells, Phys. Rev. D **64**, 035003 (2001). arXiv:hep-ph/0103067
93. H. Baer, C. Balazs, J. Ferrandis, X. Tata, Phys. Rev. D **64**, 035004 (2001). arXiv:hep-ph/0103280
94. M. Chakraborti, S. Heinemeyer, I. Saha, Eur. Phys. J. C **81**(12), 1114 (2021). arXiv:2104.03287 [hep-ph]
95. P. Cox, C. Han, T.T. Yanagida, Phys. Rev. D **104**(7), 075035 (2021). arXiv:2104.03290 [hep-ph]
96. P. Athron, C. Balázs, D.H. Jacob, W. Kotlarski, D. Stöckinger, H. Stöckinger-Kim, arXiv:2104.03691 [hep-ph]
97. F. Wang, L. Wu, Y. Xiao, J.M. Yang, Y. Zhang, arXiv:2104.03262 [hep-ph]
98. M. Chakraborti, L. Roszkowski, S. Trojanowski, JHEP **05**, 252 (2021). arXiv:2104.04458 [hep-ph]
99. J. Ellis, J.L. Evans, N. Nagata, D.V. Nanopoulos, K.A. Olive, Eur. Phys. J. C **81**(12), 1079 (2021). arXiv:2107.03025 [hep-ph]
100. J. Ellis, J.L. Evans, N. Nagata, D.V. Nanopoulos, K.A. Olive, Eur. Phys. J. C **81**(12), 1109 (2021). arXiv:2110.06833 [hep-ph]
101. S. Borsanyi et al., Nature **593**(7857), 51–55 (2021). arXiv:2002.12347 [hep-lat]
102. K. Griest, D. Seckel, Phys. Rev. D **43**, 3191 (1991)
103. J. Ellis, T. Falk, K.A. Olive, Phys. Lett. B **444**, 367 (1998). arXiv:hep-ph/9810360
104. J. Ellis, T. Falk, K.A. Olive, M. Srednicki, Astropart. Phys. **13**, 181 (2000). arXiv:hep-ph/9905481. [Erratum-ibid. **15**, 413 (2001)]
105. R. Arnowitt, B. Dutta, Y. Santoso, Nucl. Phys. B **606**, 59 (2001). arXiv:hep-ph/0102181
106. M.E. Gómez, G. Lazarides, C. Pallis, Phys. Rev. D **D61**, 123512 (2000). arXiv:hep-ph/9907261
107. M.E. Gómez, G. Lazarides, C. Pallis, Phys. Lett. B **487**, 313 (2000). arXiv:hep-ph/0004028
108. M.E. Gómez, G. Lazarides, C. Pallis, Nucl. Phys. B **B638**, 165 (2002). arXiv:hep-ph/0203131
109. T. Nihei, L. Roszkowski, R. Ruiz de Austri, JHEP **0207**, 024 (2002). arXiv:hep-ph/0206266
110. M. Citron, J. Ellis, F. Luo, J. Marrouche, K.A. Olive, K.J. de Vries, Phys. Rev. D **87**(3), 036012 (2013). arXiv:1212.2886 [hep-ph]
111. N. Desai, J. Ellis, F. Luo, J. Marrouche, Phys. Rev. D **90**(5), 055031 (2014). arXiv:1404.5061 [hep-ph]
112. C. Boehm, A. Djouadi, M. Drees, Phys. Rev. D **62**, 035012 (2000). arXiv:hep-ph/9911496
113. J.R. Ellis, K.A. Olive, Y. Santoso, Astropart. Phys. **18**, 395 (2003). arXiv:hep-ph/0112113
114. J.L. Diaz-Cruz, J.R. Ellis, K.A. Olive, Y. Santoso, JHEP **0705**, 003 (2007). arXiv:hep-ph/0701229
115. M.A. Ajaib, T. Li, Q. Shafi, Phys. Rev. D **85**, 055021 (2012). arXiv:1111.4467 [hep-ph]
116. J. Harz, B. Herrmann, M. Klasen, K. Kovarik, Q.L. Boulc'h, Phys. Rev. D **87**(5), 054031 (2013). arXiv:1212.5241

117. J. Ellis, K.A. Olive, J. Zheng, Eur. Phys. J. C **74**, 2947 (2014). arXiv:1404.5571 [hep-ph]
118. S. Raza, Q. Shafi, C.S. Ün, Phys. Rev. D **92**(5), 055010 (2015). arXiv:1412.7672 [hep-ph]
119. A. Ibarra, A. Pierce, N.R. Shah, S. Vogl, Phys. Rev. D **91**(9), 095018 (2015). arXiv:1501.03164 [hep-ph]
120. S. Mizuta, M. Yamaguchi, Phys. Lett. B **298**, 120 (1993). arXiv:hep-ph/9208251
121. J. Edsjo, P. Gondolo, Phys. Rev. D **56**, 1879 (1997). arXiv:hep-ph/9704361
122. H. Baer, C. Balazs, A. Belyaev, JHEP **0203**, 042 (2002). arXiv:hep-ph/0202076
123. A. Birkedal-Hansen, E.H. Jeong, JHEP **0302**, 047 (2003). arXiv:hep-ph/0210041
124. J. Edsjo, M. Schelke, P. Ullio, P. Gondolo, JCAP **0304**, 001 (2003). arXiv:hep-ph/0301106
125. H. Baer, M. Brhlik, Phys. Rev. D **53**, 597 (1996). arXiv:hep-ph/9508321
126. H. Baer, M. Brhlik, Phys. Rev. D **57**, 567 (1998). arXiv:hep-ph/9706509
127. H. Baer, M. Brhlik, M.A. Diaz, J. Ferrandis, P. Mercadante, P. Quintana, X. Tata, Phys. Rev. D **63**, 015007 (2001). arXiv:hep-ph/0005027
128. J.R. Ellis, T. Falk, G. Ganis, K.A. Olive, M. Srednicki, Phys. Lett. B **510**, 236 (2001). arXiv:hep-ph/0102098
129. M. Dine, D. MacIntire, Phys. Rev. D **46**, 2594 (1992). arXiv:hep-ph/9205227
130. L. Randall, R. Sundrum, Nucl. Phys. B **557**, 79 (1999). arXiv:hep-th/9810155
131. G.F. Giudice, M.A. Luty, H. Murayama, R. Rattazzi, JHEP **9812**, 027 (1998). arXiv:hep-ph/9810442
132. A. Pomarol, R. Rattazzi, JHEP **9905**, 013 (1999). arXiv:hep-ph/9903448
133. J.A. Bagger, T. Moroi, E. Poppitz, JHEP **0004**, 009 (2000). arXiv:hep-th/9911029
134. P. Binetruy, M.K. Gaillard, B.D. Nelson, Nucl. Phys. B **604**, 32 (2001). arXiv:hep-ph/0011081
135. N. Metropolis, A.W. Rosenbluth, M.N. Rosenbluth, A.H. Teller, E. Teller, J. Chem. Phys. **21**, 1087–1092 (1953). https://doi.org/10.1063/1.1699114
136. W.K. Hastings, Biometrika **57**, 97–109 (1970). https://doi.org/10.1093/biomet/57.1.97
137. N. Arkani-Hamed, A. Delgado, G.F. Giudice, Nucl. Phys. B **741**, 108–130 (2006). arXiv:hep-ph/0601041
138. H. Baer, A. Mustafayev, E.K. Park, X. Tata, JCAP **01**, 017 (2007). arXiv:hep-ph/0611387
139. R.L. Workman (Particle Data Group), PTEP **2022**, 083C01 (2022)
140. R. Ajaj et al. (DEAP Collaboration), Phys. Rev. D **100**(2), 022004 (2019). arXiv:1902.04048 [astro-ph.CO]
141. J. Ellis, N. Nagata, K.A. Olive, Eur. Phys. J. C **78**(7), 569 (2018). arXiv:1805.09795 [hep-ph]
142. J.R. Ellis, K.A. Olive, C. Savage, Phys. Rev. D **77**, 065026 (2008). arXiv:0801.3656 [hep-ph]
143. C. Amole et al. (PICO Collaboration), Phys. Rev. D **100**(2), 022001 (2019). arXiv:1902.04031 [astro-ph.CO]
144. M.L. Ahnen et al. (MAGIC and Fermi-LAT Collaborations), JCAP **02**, 039 (2016). arXiv:1601.06590 [astro-ph.HE]
145. M.L. Ahnen et al. (MAGIC Collaboration), JCAP **03**, 009 (2018). arXiv:1712.03095 [astro-ph.HE]
146. A. Albert et al. (HAWC Collaboration), Astrophys. J. **853**(2), 154 (2018). arXiv:1706.01277 [astro-ph.HE]
147. A. Albert et al. (HAWC Collaboration), Phys. Rev. D **101**(10), 103001 (2020). arXiv:1912.05632 [astro-ph.HE]
148. H. Abdallah et al. (H.E.S.S. Collaboration), Phys. Rev. D **102**(6), 062001 (2020). arXiv:2008.00688 [astro-ph.HE]
149. H. Abdallah et al. (H.E.S.S. Collaboration), Phys. Rev. Lett. **120**(20), 201101 (2018). arXiv:1805.05741 [astro-ph.HE]
150. K. Choi et al. (Super-Kamiokande Collaboration), Phys. Rev. Lett. **114**(14), 141301 (2015). arXiv:1503.04858 [hep-ex]
151. S. Adrian-Martinez et al. (ANTARES Collaboration), Phys. Lett. B **759**, 69–74 (2016). arXiv:1603.02228 [astro-ph.HE]
152. A. Albert et al. (HAWC Collaboration), Phys. Rev. D **98**, 123012 (2018). arXiv:1808.05624 [hep-ph]
153. T. Sjostrand, S. Mrenna, P.Z. Skands, JHEP **05**, 026 (2006). https://doi.org/10.1088/1126-6708/2006/05/026. arXiv:hep-ph/0603175
154. T. Sjöstrand, S. Ask, J.R. Christiansen, R. Corke, N. Desai, P. Ilten, S. Mrenna, S. Prestel, C.O. Rasmussen, P.Z. Skands, Comput. Phys. Commun. **191**, 159–177 (2015). https://doi.org/10.1016/j.cpc.2015.01.024. arXiv:1410.3012 [hep-ph]
155. L. Bergstrom, P. Ullio, J.H. Buckley, Astropart. Phys. **9**, 137–162 (1998). arXiv:astro-ph/9712318
156. P. Ullio, L. Bergstrom, J. Edsjo, C.G. Lacey, Phys. Rev. D **66**, 123502 (2002). arXiv:astro-ph/0207125
157. Y. Mambrini, C. Munoz, Astropart. Phys. **24**, 208–230 (2005). arXiv:hep-ph/0407158
158. J.F. Navarro, C.S. Frenk, S.D.M. White, Astrophys. J. **490**, 493–508 (1997). https://doi.org/10.1086/304888. arXiv:astro-ph/9611107
159. A. Burkert, Astrophys. J. Lett. **447**, L25 (1995). https://doi.org/10.1086/309560. arXiv:astro-ph/9504041
160. C. Dessert, J.W. Foster, Y. Park, B.R. Safdi, W.L. Xu, arXiv:2207.10090 [hep-ph]
161. A. Acharyya et al. (CTA Collaboration), JCAP **01**, 057 (2021). https://doi.org/10.1088/1475-7516/2021/01/057. arXiv:2007.16129 [astro-ph.HE]
162. J. Ellis, K.A. Olive, C. Savage, V.C. Spanos, Phys. Rev. D **81**, 085004 (2010). arXiv:0912.3137 [hep-ph]
163. J. Ellis, K.A. Olive, C. Savage, V.C. Spanos, Phys. Rev. D **83**, 085023 (2011). arXiv:1102.1988 [hep-ph]
164. P. Scott et al. (IceCube Collaboration), JCAP **11**, 057 (2012). https://doi.org/10.1088/1475-7516/2012/11/057. arXiv:1207.0810 [hep-ph]
165. M.G. Aartsen et al. (IceCube Collaboration), Phys. Rev. Lett. **110**(13), 131302 (2013). https://doi.org/10.1103/PhysRevLett.110.131302. arXiv:1212.4097 [astro-ph.HE]
166. ATLAS Collaboration, https://twiki.cern.ch/twiki/bin/view/AtlasPublic/SupersymmetryPublicResults
167. A. Abada et al. (FCC Collaboration), Eur. Phys. J. C **79**(6), 474 (2019). https://doi.org/10.1140/epjc/s10052-019-6904-3